Controlled sumoylation of the mevalonate pathway enzyme HMGS-1 regulates metabolism during aging

Amir Sapir[a,b], Assaf Tsur[c], Thijs Koorman[d], Kaitlin Ching[a,b], Prashant Mishra[a], Annabelle Bardenheier[a,b], Lisa Podolsky[c], Ulrike Bening-Abu-Shach[c], Mike Boxem[d], Tsui-Fen Chou[e], Limor Broday[c,1], and Paul W. Sternberg[a,b,1]

[a]Division of Biology and Biological Engineering and [b]Howard Hughes Medical Institute, California Institute of Technology, Pasadena, CA 91125; [c]Department of Cell and Developmental Biology, Sackler School of Medicine, Tel Aviv University, Tel Aviv 69978, Israel; [d]Developmental Biology, Utrecht University, 3584 CH, Utrecht, The Netherlands; and [e]Division of Medical Genetics, Department of Pediatrics, and Los Angeles Biomedical Research Institute, Harbor–UCLA Medical Center, Torrance, CA 90502

Contributed by Paul W. Sternberg, August 6, 2014 (sent for review July 3, 2014)

Many metabolic pathways are critically regulated during development and aging but little is known about the molecular mechanisms underlying this regulation. One key metabolic cascade in eukaryotes is the mevalonate pathway. It catalyzes the synthesis of sterol and nonsterol isoprenoids, such as cholesterol and ubiquinone, as well as other metabolites. In humans, an age-dependent decrease in ubiquinone levels and changes in cholesterol homeostasis suggest that mevalonate pathway activity changes with age. However, our knowledge of the mechanistic basis of these changes remains rudimentary. We have identified a regulatory circuit controlling the sumoylation state of *Caenorhabditis elegans* HMG-CoA synthase (HMGS-1). This protein is the ortholog of human HMGCS1 enzyme, which mediates the first committed step of the mevalonate pathway. In vivo, HMGS-1 undergoes an age-dependent sumoylation that is balanced by the activity of ULP-4 small ubiquitin-like modifier protease. ULP-4 exhibits an age-regulated expression pattern and a dynamic cytoplasm-to-mitochondria translocation. Thus, spatiotemporal ULP-4 activity controls the HMGS-1 sumoylation state in a mechanism that orchestrates mevalonate pathway activity with the age of the organism. To expand the HMGS-1 regulatory network, we combined proteomic analyses with knockout studies and found that the HMGS-1 level is also governed by the ubiquitin–proteasome pathway. We propose that these conserved molecular circuits have evolved to govern the level of mevalonate pathway flux during aging, a flux whose dysregulation is associated with numerous age-dependent cardiovascular and cancer pathologies.

HMG-CoA synthase | sterol synthesis | yeast two-hybrid

Many metabolic pathways are critically regulated during development and aging, but little is known about the molecular mechanisms underlying this regulation. The mevalonate pathway is a key metabolic cascade that converts acetyl-CoA and acetoacetyl-CoA to farnesyl diphosphate, a precursor of sterol isoprenoids such as cholesterol, steroid hormones, and bile acids. In addition, farnesyl diphosphate feeds into cascades that synthesize nonsterol isoprenoids, such as heme-A and ubiquinone, required for electron transfer during respiration (1). Moreover, the mevalonate pathway catalyzes the synthesis of essential intermediates for tRNA modification, protein glycosylation, and protein prenylation. Protein prenylation is a requisite step in the activation of proteins involved in many intracellular signaling pathways that control cell growth and differentiation. For example, prenylation of small G proteins from the Ras, Rho, and Rac superfamilies dictates the membrane localization of these proteins that is essential for their activation (2). Although the main trunk of the pathway is conserved in eukaryotes, some of the downstream branches vary between organisms. In fungi the main structural sterol produced by the pathway is ergosterol instead of cholesterol in vertebrates, whereas in some invertebrates, including *Caenorhabditis elegans*, the sterol synthesis branch is absent (3).

Many cellular processes and physiological states rely on variable levels of mevalonate pathway metabolites, suggesting that the pathway activity is highly regulated during the organism's life cycle. Elucidating the molecular details of this regulation is the first step in understanding how pathway dysregulation leads to diseases. For example, as part of the tumorigenic process of breast cancer cells, the expression of many mevalonate pathway enzymes is up-regulated by a mutant p53 protein (4). This overactivation of the mevalonate pathway is both necessary and sufficient to induce the mutant p53 phenotype in cancerous breast tissue architecture. Studies of mevalonate pathway regulation have primarily focused on regulators of HMG-CoA reductase (HMGCR), which converts HMG-CoA into mevalonate (5). HMGCR catalyzes the primary rate-limiting step of the mevalonate pathway and is therefore highly regulated by transcriptional and posttranscriptional control (6). The regulation of other enzymes in the pathway is largely unexplored, but growing evidence suggests that enzymes beyond HMGCR can serve as flux-controlling points (7). One potential regulatory node is the first committed enzyme of the pathway, HMG-CoA synthase (HMGCS1). This cytoplasmic enzyme mediates the condensation of acetyl-CoA and acetoacetyl-CoA to HMG-CoA. *hmgcs1* transcription is highly controlled by cholesterol levels in humans (8). In addition, whole-proteome studies of posttranslational modifications have identified specific HMGCS1 residues that undergo phosphorylation (9), acetylation (10), and ubiquitination (11–13). These findings suggest that HMGCS1 undergoes

Significance

The mevalonate pathway plays a critical role in cholesterol homeostasis and cancer development, two major challenges in modern medicine. Consequently, cholesterol-reducing medications (statins) that target this pathway are the best-selling pharmaceutical drugs in history. Beyond regulation of the enzyme HMG-CoA reductase, little is known about additional posttranslational regulatory nodes in the mevalonate pathway or how this cascade is controlled with age. We have discovered a regulatory circuit that controls HMGS-1, the first enzyme of the mevalonate pathway, during aging. HMGS-1 is regulated by posttranslational ubiquitination and age-dependent sumoylation. Sumoylation is reversed by the spatiotemporally controlled activity of a specific small ubiquitin-like modifier protease. This conserved molecular circuit could serve as a handle for targeting the mevalonate pathway in future therapeutics.

Author contributions: A.S., M.B., T.-F.C., L.B., and P.W.S. designed research; A.S., A.T., T.K., K.C., P.M., A.B., L.P., U.B.-A.-S., T.-F.C., and L.B. performed research; A.S., A.T., T.K., P.M., M.B., T.-F.C., and L.B. analyzed data; and A.S., K.C., L.B., and P.W.S. wrote the paper.

The authors declare no conflict of interest.

[1]To whom correspondence may be addressed. Email: pws@caltech.edu or broday@post.tau.ac.il.

This article contains supporting information online at www.pnas.org/lookup/suppl/doi:10.1073/pnas.1414748111/-/DCSupplemental.

complex posttranslational regulation, but the biological significance of these modifications remains unclear.

Among the growing family of ubiquitin-like modifiers (UBLs), ubiquitin and small ubiquitin-like modifier (SUMO) are the most studied proteins. These two proteins share analogous enzymatic cascades that mediate, as a final step, covalent conjugation of the modifier to lysine residues of the substrate. In contrast to the canonical role of ubiquitin as mediator of protein degradation, conjugation of SUMO (sumoylation) can alter protein activity, localization, and stability without directly causing degradation. SUMO has emerged as a critical regulator in a variety of processes including cell cycle regulation, transcription, nuclear architecture control, chromosome stability regulation, and subcellular transport (14, 15). So far, the role of sumoylation in metabolic control has been attributed primarily to its transcriptional regulation activity, as in the regulation of the metabolic transcription factor HIF-1a. However, SUMO is also conjugated to the mitochondria fission protein DRP-1 (16), and some metabolic enzymes have been identified among the pool of potential SUMO targets (17). These findings suggest that SUMO might play a direct role in metabolic regulation. SUMO modification is a highly dynamic and reversible process in part due to the activity of ubiquitin-like proteases (ULPs) and sentrin-specific proteases (SENPs) that cleave SUMO from the substrate (18). This highly conserved family of cysteine proteases includes Ulp1 and Ulp2 of *Saccharomyces cerevisiae*; ULP-1, ULP-2, ULP-4, and ULP-5 of *C. elegans*; and SENP1– SENP3 and SENP5–SENP7 of humans (18, 19). SUMO proteases share the same domain organization of a conserved catalytic domain close to the C-terminal end and a variable N-terminal domain that dictates the protease subcellular localization and substrate recognition. Studies in yeast and mammals have revealed that most SENPs localize to the nucleus in recognizable subnuclear compartments (18). In recent years, however, emerging data have demonstrated that some SENPs/ULPs also localize to the cytoplasm and intracellular organelle surfaces. For example, Ulp1 localizes primarily in the nuclear pore complex but translocates to the cytoplasm in a cell cycle-specific manner (20). Even more strikingly, SENP5 localization cycles between the nucleus and the outer surface of the mitochondria. At the mitochondria, it regulates organelle morphology by controlling the sumoylation state of the mitochondria fission protein DRP-1 (21). Beyond these few cases, the role of SENPs/ULPs in the regulation of cytoplasmic and mitochondrial processes has yet to be explored.

Here we describe a previously unidentified regulatory circuit that orchestrates HMGS-1 levels with age. We found that HMGS-1 undergoes an age-dependent sumoylation that is temporally balanced by the activity of ULP-4 SUMO protease. In addition to a role for sumoylation, we discovered that the ubiquitin–proteasome system also controls HMGS-1 levels. Evolutionary conservation of both mechanisms suggests that this regulatory network is fundamental to mevalonate pathway activity in eukaryotes. Our findings place the first committed enzyme of the pathway as a target for complex posttranslational regulation.

Results

ULP-4 SUMO Protease Exhibits Cytoplasm-to-Mitochondria Translocation. As a first step in the study of SUMO proteases' role in whole-organism development, we have focused on the family of *C. elegans* ULPs (Fig. S1). In the process of exploring the expression patterns of these ULPs, we found that a GFP-labeled ULP-4 exhibits a developmentally regulated expression pattern that is dependent on tissue type and worm age (Fig. 1). Notably, ULP-4::GFP rescues *ulp-4* deletion mutant phenotypes (see ulp-4 *Mutant Worms Are Metabolically Impaired*); furthermore, its GFP signal is reduced by *ulp-4* RNAi (Fig. S2). These suggest that the construct represents endogenous ULP-4 activity. *ulp-4* expression initiates in body wall muscles (BWMs) and hypodermal cells during embryonic development (Fig. 1 *A–C*) and is maintained throughout the worm's life (Fig. 1 *D–H*). During the development from larval stages 1–3, *ulp-4* is expressed in the pharynx and hypodermis (Fig. 2*D*). A second phase of *ulp-4* expression in BWMs and

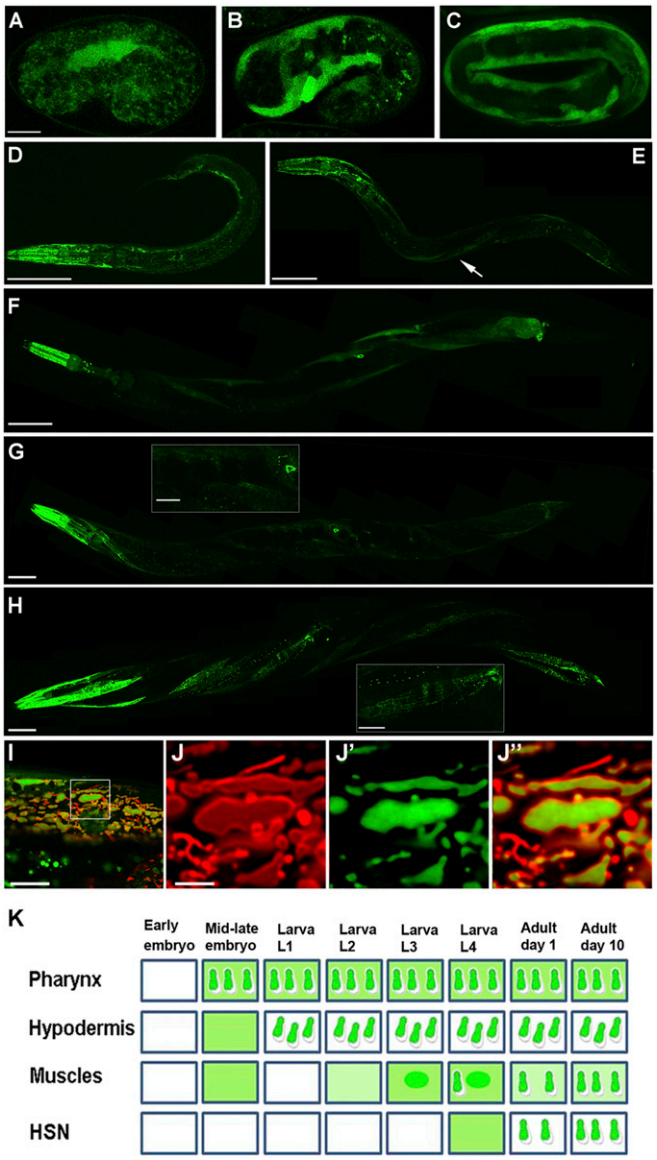

Fig. 1. ULP-4 exhibits a cytosol-to-mitochondria translocation. (*A–C*) ULP-4 expression initiates at midembryogenesis in muscles. ULP-4 protein is distributed in the cytoplasm. (*D*) ULP-4 protein cytoplasm-to-mitochondria translocation in hypodermal cells at L1 stage. Pharyngeal cells also start to express ULP-4 that is sorted to the mitochondria. (*E*) At L3 BWM cells express ULP-4 as a cytoplasmic protein (arrow). (*F*) At L4, ULP-4 expression initiates at the HSNs concomitant with ULP-4 translocation to the mitochondria of head and tail muscles. (*G*) Day-1 adult worms exhibit mitochondrial localization of ULP-4 in HSNs and most of the BWM cells. *G*, *Inset* shows a muscle anterior to the HSN soma where ULP-4 is still cytoplasmic. (*H*) In day-10 adult worms, ULP-4 localizes to the mitochondria of all muscle cells. *H*, *Inset* shows mitochondrial ULP-4 in the region as in *G*. (*I–J″*) Colocalization of ULP-4 with the mitochondrial outer membrane marker TOM-20::mRFP in muscles demonstrates ULP-4 matrix localization. (*I*) A merged image of a single muscle cell. (*J–J″*) A single organelle analysis of TOM-20:mRFP distribution (*J*), ULP-4::GFP localization (*J′*), and merged distributions (*J″*). (*K*) A comprehensive diagram of ULP-4 expression and localization pattern. In all experiments, $n \geq 15$ worms. (Scale bars: 10 μm in *A–C*, 50 μm in *D–H*, 10 μm in G and H *Insets*, 10 μm in *I*, and 2.5 μm in *J*.)

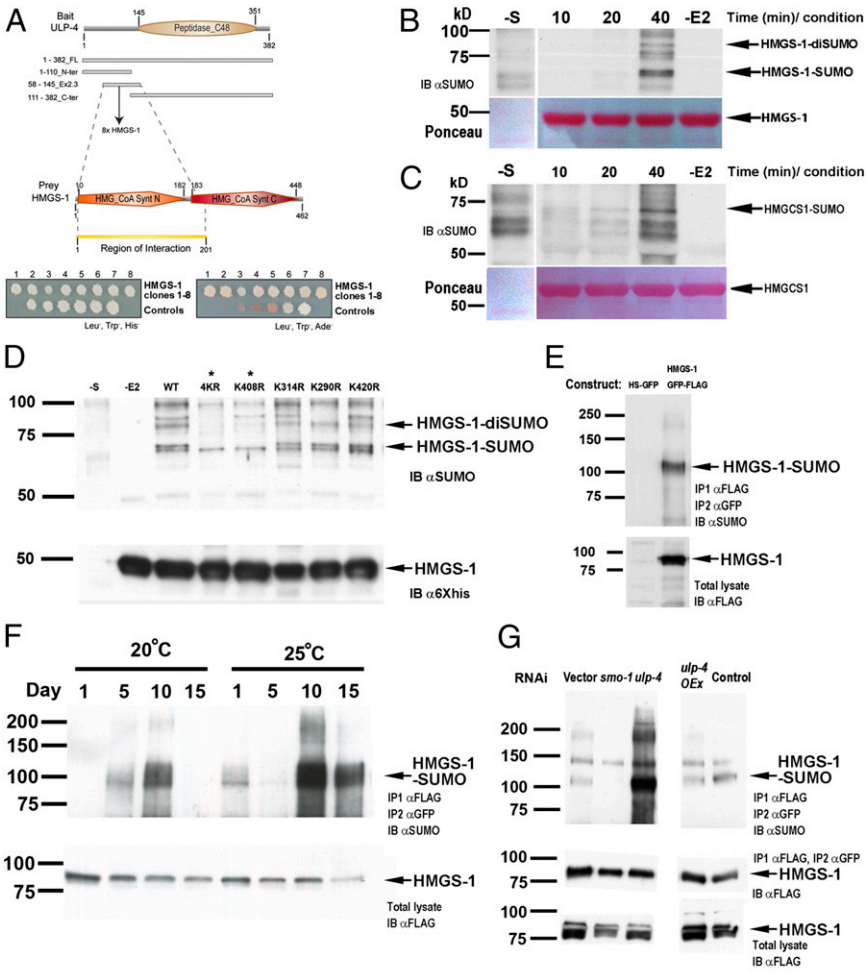

Fig. 2. HMGS-1 is sumoylated in an age-dependent manner in vivo. (*A*) ULP-4 and HMGS-1 protein fragments interact in a yeast two-hybrid assay. (*B*–*D*) In vitro sumoylation reactions. Lanes labeled with −E2 are control reactions in which UBC9 is absent and −S are controls in which substrate is absent. (*B*) Time course (in minutes) of HMGS-1 sumoylation. (*C*) Similar to HMGS-1, human HMGCS1 is sumoylated in vitro. (*D*) The sumoylation pattern of WT and various lysine-to-arginine HMGS-1 mutants constructed based on sumoylation prediction (Fig. S4*A*). 4KR is a HMGS-1 variant whose four predicted sumoylated lysines were mutated to arginines. Arrows mark the sumoylated-HMGS-1 bands, and asterisks label sumoylation-abolished HMGS-1 variants. (*E*) An assay for HMGS-1 sumoylation detection in vivo. IB, immunoblot. (*F*) HMGS-1 sumoylation increases with age and temperature until day 10 of adulthood. Total levels of HMGS-1 were determined by HMGS-1::FLAG::GFP detection from the total lysates. (*G*) ULP-4 knockdown resulted in increased HMGS-1 sumoylation whereas ULP-4 overexpression (*ulp-4* OEx) resulted in a mild decrease of HMGS-1 sumoylation.

hermaphroditic-specific neurons (HSNs) starts at L4 stage (Fig. 1*F*) and continues through adulthood (Fig. 1 *G* and *H*). Although the ULP-4 localization pattern varies between tissue types, we found a common pattern of subcellular localization with time. In each tissue, ULP-4 protein initially localizes to the cell's nucleus and cytoplasm but accumulates later in development in intracellular compartments that resemble mitochondria (Fig. 1*K*). We confirmed the mitochondrial localization by colocalization of ULP-4::GFP with TOM-20::mRFP, a protein that labels the outer mitochondria membrane (Fig. 1 *I* and *J*). High-resolution optical cross-sections through the organelle suggest that ULP-4 accumulates in the mitochondrial matrix. Likely, this age-regulated subcellular localization determines ULP-4 substrate specificity by changing its site of action.

ULP-4 Interacts with *C. elegans* HMGS-1. Identification of substrates is crucial for understanding the role of SENPs/ULPs in cellular processes. Intrigued by the ULP-4 localization pattern, we screened *C. elegans* two-hybrid libraries to identify potential substrates. Because the N-terminal portion of many SENPs/ULPs has been identified as the substrate recognition domain (22), we used different regions of this domain as bait (Fig. 2*A*). The screen revealed eight independent interaction events between ULP-4 and the HMGS-1 protein (Fig. 2*A*). *C. elegans* HMGS-1 is the ortholog of two metabolic enzymes of mammals: HMGCS1 and HMGCS2. HMGCS1 is the first committed enzyme of the mevalonate pathway (3), whereas HMGCS2 functions in ketone body synthesis (23). Reports about ketone body metabolism in invertebrates are scarce (24, 25), so we focused on whether HMGS-1 is required for mevalonate pathway metabolism. *hmgs-1* RNAi induces strong and robust phenotypes including paralysis, reduced pharyngeal pumping, and sterility (Fig. S3*B* and Movie S1). In agreement with previous reports on the involvement of *hmgs-1* in the mevalonate pathway (26, 27), these *hmgs-1* RNAi phenotypes were fully rescued by mevalonate supplementation, indicating that *C. elegans* HMGS-1 is functionally equivalent to its ortholog HMGCS1 (Fig. S3*B* and Movie S2).

HMGS-1 Is Sumoylated in Vitro at Lys408. The interaction between ULP-4 SUMO protease and HMGS-1 suggests that HMGS-1 is sumoylated. To understand the molecular details of HMGS-1

modification, we first tested whether HMGS-1 is sumoylated in vitro. We found that a recombinant, bacterial-expressed *C. elegans* HMGS-1 protein is efficiently sumoylated in vitro when incubated with human SUMO-1, E1, UBC9, and ATP (Fig. 2*B*). To examine a possible evolutionary conservation of this mechanism, we used the same in vitro sumoylation assay on recombinant human HMGCS1 and found that it is also sumoylated. This observation suggests that this mode of regulation is evolutionarily conserved in humans (Fig. 2*C*). To identify the sumoylated residue, we surveyed the HMGS-1 protein sequence for predicted sumoylation sites. Of the 27 HMGS-1 lysines, sumoylation site prediction programs identified four potential sites (Fig. S4*A*). In agreement with this prediction, the HMGS-1 sumoylation level was reduced when we mutated all four predicted lysines to arginines (Fig. 2*D*). Single Lys-to-Arg mutations pinpointed the sumoylated residue as Lys408. Lys408 is a strong candidate to be the site of HMGS-1 sumoylation in vivo as it has the highest sumoylation prediction score and is sumoylated in vitro. Moreover, this residue is conserved in the mammalian HMGCS1 sequence, and undergoes ubiquitination (12) (Figs. S4*B* and S5). This conservation may represent an evolutionarily conserved cross-talk between sumoylation and ubiquitination. Sumoylation of Lys408 might protect the protein from ubiquitination that occurs at the same site (28), or it might elicit sumoylation-dependent ubiquitination (e.g., ref. 29).

In Vivo, HMGS-1 Is Sumoylated in an Age-Dependent Manner. To test whether *C. elegans* HMGS-1 is sumoylated in vivo, we immunoprecipitated a GFP-3×FLAG-tagged version of HMGS-1 and assessed its sumoylation state by anti-SUMO antibodies (Fig. 2*E*). We found that HMGS-1 is sumoylated when the cultures include worms grown for at least 4 d as gravid adults (Fig. 2*F*). The size shift of the modified HMGS-1 is about 20 kDa, corresponding to monosumoylation. The fact that HMGS-1 sumoylation was detected only in cultures with worms older than day-4 gravid adult suggests that HMGS-1 is being sumoylated in an age-dependent manner. To test the dynamics of HMGS-1 SUMO conjugation, we grew synchronized, sterile cultures of worms and examined the degree of HMGS-1 sumoylation in 5-d intervals during adulthood. Strikingly, we found that the level of HMGS-1 sumoylation increases with age from day 1 of adulthood (no detectable sumoylation) until day 10 (maximum sumoylation; Fig. 2*F*). To test the possible effect of environmental conditions on HMGS-1 modification, we repeated the analysis on synchronized cultures grown at 25 °C, a mild stress condition. We found the same pattern of age-dependent HMGS-1 modification; however, the level of HMGS-1 sumoylation increased relative to worms of the same age grown at 20 °C. This suggests that environmental factors that change the physiological state of the organism can also change the level of HMGS-1 modification. Worms fed with *smo-1* RNAi exhibited an almost complete elimination of the SUMO band, demonstrating the specificity of this assay (Fig. 2*G*). To study the effect of ULP-4 activity on the HMGS-1 modification state, we knocked down ULP-4 SUMO protease by RNAi. Strikingly, this knockdown resulted in an increased level of HMGS-1 sumoylation in vivo (Fig. 2*G*). This finding accords with both the interaction between HMGS-1 and ULP-4 found in the two-hybrid screen and the proposed enzymatic activity of ULP-4 as a SUMO protease. Taken together, these results reveal a previously unidentified molecular circuit in which controlled activity of ULP-4 SUMO protease balances the level of HMGS-1 sumoylation.

***ulp-4* Mutant Worms Are Metabolically Impaired.** To unveil the function of ULP-4 SUMO protease, we characterized the phenotypes resulting from a deletion in the *ulp-4* locus. This allele introduces a frame shift followed by a stop codon at the beginning of exon 4 (Fig. S6), presumably resulting in a severe decrease of ULP-4 function. Worms homozygous for this allele are viable but exhibit phenotypes associated with impaired metabolism. *ulp-4* mutants are almost completely sterile; furthermore, their pumping rate and locomotion undergo a notable decline with age (Fig. 3*A*). In addition, *ulp-4* mutants have significantly less fat (Fig. S6*C*). This effect can be partially rescued by the ULP-4::GFP construct, demonstrating that these phenotypes stem from ULP-4 loss. Remarkably, these phenotypes show a strong age dependency consistent with *ulp-4* age-dependent expression as well as with the proposed role of ULP-4 as a regulator of the mevalonate pathway. Consistent with this observation, *ulp-4* mutant worms are long-lived, whereas ULP-4::GFP worms, in which ULP-4 is mildly overexpressed, are short-lived (Fig. S7).

Through ubiquinone and heme-A synthesis, mevalonate pathway flux is directly required for proper electron transport (Fig. S3*A*). To examine the possible effect of *ulp-4* loss on mitochondria homeostasis, we measured the degree of mitochondria membrane potential and respiration. *ulp-4* mutant mitochondria fail to maintain normal membrane potential as determined by tetramethylrhodamine ethyl ester (TMRE) staining (Fig. 3*D*). In addition, *ulp-4* loss results in decreased oxygen consumption relative to WT worms (Fig. 3*E*), whereas ULP-4::GFP worms consume more oxygen than WT worms. Dysregulation of the mevalonate pathway likely impairs mitochondrial electron transport rate by affecting coenzyme Q production, thereby affecting lifespan and the rate of respiration (30). Although ULP-4 probably has many targets, it is possible that the *ulp-4* mutant phenotypes described above stem, at least in part, from dysregulated HMGS-1 activity. To examine this hypothesis, we tried to rescue the *ulp-4* loss of function phenotypes by adding mevalonate exogenously. Indeed, mevalonate supplementation rescues *ulp-4* mutants' reduction of pumping in a dosage-dependent manner, whereas only marginally affecting the pumping rates of WT worms (Fig. 3*C*). Taken together, these results show the role ULP-4 plays in controlling the mevalonate pathway and worm metabolism. A partial rescue of *ulp-4* mutant phenotypes by mevalonate demonstrates that oversumoylated HMGS-1 is less active, placing ULP-4 as a positive regulator of HMGS-1 activity. This uncovers the mechanistic basis by which HMGS-1 sumoylation and ULP-4–mediated desumoylation control the mevalonate pathway.

HMGS-1 Interacts with the Ubiquitin–Proteasome Pathway. To characterize the molecular circuits that control HMGS-1 more comprehensively, we searched for HMGS-1 interactors by immunoprecipitation (IP), followed by mass spectrometry (MS) analysis. We identified 663 proteins that were enriched in an HMGS-1–immunoprecipitated fraction in comparison with the control (Dataset S1). The list of HMGS-1 interactors was enriched in five Kyoto Encyclopedia of Genes and Genomes (KEGG, www.genome.jp/kegg) pathways (Fig. 4*A* and Fig. S8). Three of these (valine/leucine/isoleucine degradation, citrate cycle, and propanoate metabolism) feed substrates into the mevalonate pathway (acetyl-CoA or acetoacetyl-CoA, explicitly) that are metabolized by HMGS-1. This raises the possibility that HMGS-1 functions as part of a high-order metabolic scaffold (Fig. 4*A*). A fifth enriched pathway is ubiquitin–proteasome, which may lead to degradation of HMGS-1. Strikingly, 20 proteins that coprecipitated with HMGS-1 are in the broader ubiquitin–proteasome pathway (Fig. S8). These include an E2 ubiquitin carrier (UBC-13), an ubiquitin fusion degradation enzyme (UFD-1), a proteasomal ubiquitin adaptor (ADRM-1–like) (31), and an ubiquitin carboxyl-terminal hydrolase UBH-4. To test the potential role of HMGS-1 ubiquitination, these interactors were knocked down by RNAi. Knockdown of either UBA-5 or UBC-13 interactors resulted in an increased HMGS-1::GFP signal in comparison with an empty vector control (Fig. 4*B*). This demonstrates a role of the ubiquitin pathway in HMGS-1 regulation. To examine whether the identified HMGS-1 regulatory

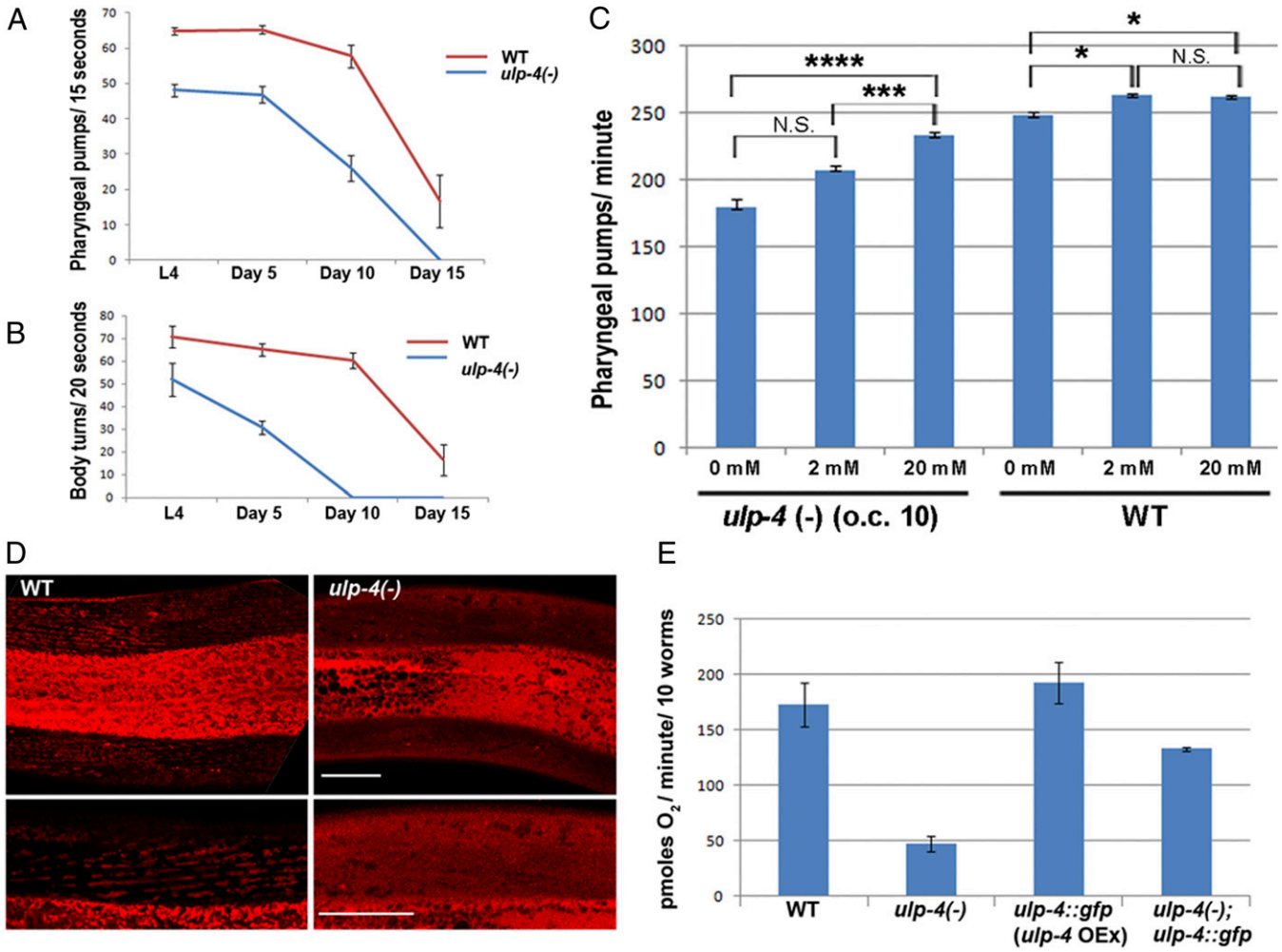

Fig. 3. ULP-4 loss results in age-dependent metabolic phenotypes. (*A*) Pharyngeal pumping rate is reduced in *ulp-4(-)* mutant worms relative to the pumping rate of WT worms. (*B*) *ulp-4(-)* worms exhibit an accelerated age-dependent reduction of locomotion. (*C*) Nutritional supplementation of mevalonate rescues the *ulp-4(-)* mutant phenotype. Worms were grown at 20 °C and tested at day 1 of adulthood. Error bars represent SEs. $*P \leq 0.05$, $**P \leq 0.01$, $***P \leq 0.001$, $****P \leq 0.0001$. (*D*) Lack of TMRE accumulation demonstrates that mitochondria homeostasis is impaired in worms lacking *ulp-4*. (Scale bars: 20 μm) (*E*) ULP-4 activity is required for proper respiration. *ulp-4(-)* worms exhibit a significant reduction in oxygen consumption. This reduction was rescued by the ULP-4::GFP construct described in Fig. 1.

network is conserved in sterol-producing organisms, we searched the protein–protein interaction database Biological General Repository for Interaction Datasets (http://thebiogrid.org) (32). Consistent with our findings in *C. elegans*, the HMGS-1 ortholog ERG13 of the sterol-producing yeast *S. cerevisiae* is suggested to be both sumoylated (33) and ubiquitinated (34). ERG-13 interacts with ubiquitin (UBI4), ubiquitin-specific protease (UBP3), SUMO (SMT3), and a SUMO protease (ULP1) (35) (Fig. 4*D*), as well as with various proteasomal subunits. So far, only a small set of interactors have been identified for HMGCS1, the human ortholog of HMGS-1. Although limited in number, the pool of HMGCS1 interactors includes the polyubiquitin-C protein (11, 12). High throughput screens have suggested that human HMGCS1 undergoes ubiquitination at multiple sites (Fig. S4), but the outcome of this modification is not yet clear. This interaction and our finding that HMGCS1 is sumoylated in vitro suggest that this regulatory circuit is also conserved in humans.

A Model for the HMGS-1 Regulatory Circuit. Collectively, the molecular, genetic, and metabolic data suggest a model in which HMGS-1 activity is governed by two modes of posttranslational modification (Fig. 4*C*). We propose that the balance between HMGS-1 sumoylation and desumoylation is highly regulated during the lifespan of the organism and is used to control the level of HMGS-1 activity. This balance orchestrates HMGS-1 activity with respect to tissue type, developmental stage, and the organism's age. Early in the development of *C. elegans*, the activity of ULP-4 in the cytoplasm results in less sumoylated and presumably more active HMGS-1. As the worm ages, mitochondrial sequestration of ULP-4 results in HMGS-1 oversumoylation and inactivation (Fig. 4*D*). In addition, the ubiquitin–proteasome pathway also governs HMGS-1 levels, highlighting how critical control of HMGS-1 levels is. It is possible that a cross-talk between sumoylation and ubiquitination dictates HMGS-1 levels or that these two pathways are acting as two parallel branches within the HMGS-1 regulatory network. Nevertheless, these regulatory circuits not only explain how spatial and temporal control of mevalonate pathway flux evolved, they also place HMGS-1/HMGCS1 as a target for age-dependent posttranslational regulation. In addition to the dynamic control of HMGCR levels by ubiquitination (36), HMGS-1/HMGCS1 posttranslational regulation presumably plays a more long-term role in mevalonate pathway control. One potential implication of our findings is

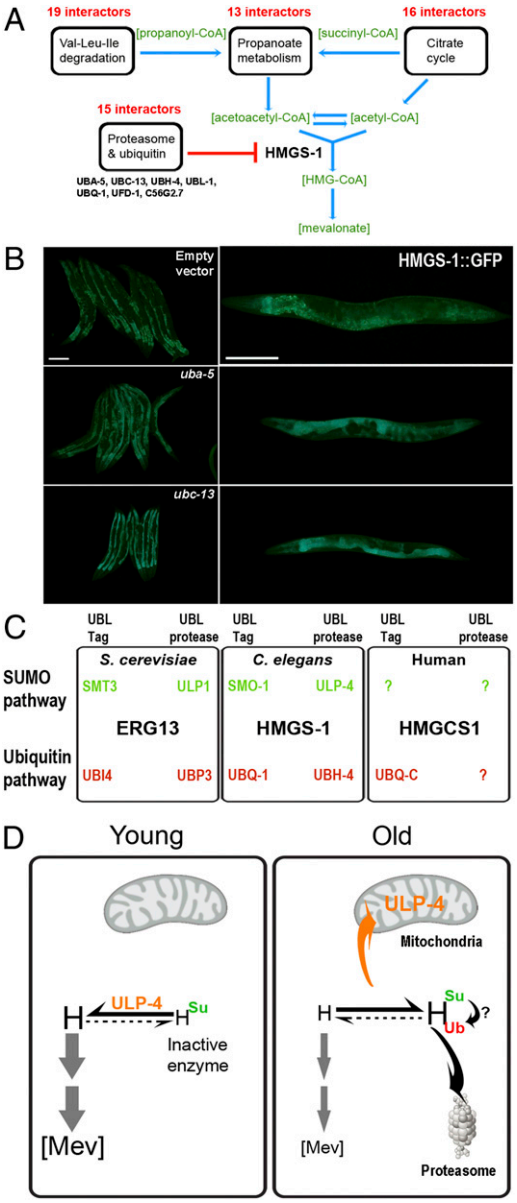

Fig. 4. HMGS-1 interaction network and a proposed regulatory circuit. (*A*) HMGS-1 interactors, revealed by HMGS-1 IP and MS. Shown are KEGG pathways significantly enriched (see also Fig. S8*A*). The four enriched metabolic pathways are involved in either acetyl-CoA or acetoacetyl-CoA metabolism suggesting that HMGS-1 is part of high-order metabolic scaffolds. Twenty proteins from the proteasome and ubiquitin pathway were also identified (Fig. S8*C*). (*B*) Worms expressing HMGS-1::GFP were subjected to RNAi against candidate genes corresponding to proteins identified as HMGS-1 interactors from the proteomic screen. Depletion of UBA-5 and UBC-13 leads to an elevated level of HMGS-1::GFP. (Scale bars: 200 μm) (*C*) A survey of protein–protein databases demonstrated that HMGS-1 regulatory network is conserved in sterol-producing organisms. UBL-Tag are either ubiquitin or SUMO modifiers and UBL-proteases are either ubiquitin or SUMO proteases. (*D*) A model for the HMGS-1 regulatory circuit. This model suggests that balance between HMGS-1 sumoylation and desumoylation affects HMSG-1 activity and mevalonate pathway flux. H, *C. elegans* HMGS-1; [Mev], mevalonate pathway flux; Su, *C. elegans* SUMO; Ub, *C. elegans* ubiquitin-A.

a mechanistic understanding of how the mevalonate pathway flux is controlled with age. We hypothesize that in humans, perturbations of this regulatory circuit may result in an age-dependent overactivation of the mevalonate pathway that leads to cholesterol overproduction and cancer progression.

Discussion

Despite their vital role in numerous cellular processes related to health and disease, little is known about posttranslational mechanisms that control the mevalonate pathway beyond HMGCR. We have applied genetic and proteomic screens along with developmental, metabolic, and biochemical approaches to discover an evolutionarily conserved mechanism that controls HMGS-1 levels. This molecular circuit includes age-dependent HMGS-1 sumoylation that is balanced by the spatiotemporally regulated activity of the ULP-4 SUMO protease. We also identified the ubiquitin–proteasome pathway as part of the HMGS-1 regulatory network and demonstrated its role in controlling HMGS-1 levels. By identifying HMGS-1 as the target for both ubiquitination and age-controlled sumoylation in vivo, we set the foundation for a mechanistic understanding of HMGS-1 posttranslational regulation within the context of the dynamic metabolism of the organism.

Studies on sumoylation were carried out primarily in single-cell systems such as yeast and mammalian cells in culture (19, 37). It is not clear how sumoylation is controlled in a whole organism with various tissue types and a complex life cycle. The unexpectedly complex but stereotypic expression and subcellular localization pattern of ULP-4 (Fig. 1) may serve as a mechanism by which SUMO proteases temporally govern developmental processes. In contrast to SENP5 that localizes at some stages of the cell cycle on the mitochondria outer surface (21), our high-resolution analyses show that ULP-4 translocates to the mitochondrial matrix (Fig. 1*K*). Although we cannot rule out the possibility that ULP-4 deconjugates sumoylated mitochondrial matrix proteins, our results suggest that localization to the mitochondrial matrix sequesters ULP-4, preventing its cytoplasmic function. The ULP-4 protein does not have a defined mitochondria-sorting signal, but it may harbor a noncanonical signal as do more than 50% of the mitochondrially sorted proteins (38). Consistent with reports on other SENPs/ULPs (20), substrate recognition by ULP-4 was dependent on its N-terminal portion (Fig. 2*A*). This region harbors a signature acidic stretch that also exists in the N-terminal portion of human SENP3 and less evidently in the ULP-4 orthologs SENP6/SENP7 (Fig. S9). This acidic stretch may play a conserved role either in subcellular sorting or in substrate recognition.

Our temporal biochemical analyses clearly show that HMGS-1 undergoes age-dependent sumoylation (Fig. 2) and that this sumoylation is regulated by the activity of an age-controlled protease (Figs. 1 and 2). Although sumoylation may be a powerful mechanism to regulate protein activity with age, only a few cases of regulated sumoylation have been reported. Global sumoylation analyses comparing 3- and 25-mo-old mice spleens revealed that a few uncharacterized proteins undergo age-enhanced sumoylation in a SUMO-1 specific manner (39). In addition, SUMO-3 conjugation is reported to play some role in age-dependent learning and memory decay. In the AβPP Tg2576 mouse model of Alzheimer's disease, SUMO-1 conjugation of a yet-to-be identified substrate increased at 3 and 6 mo in comparison with 1.5 mo of age (40). To our knowledge, age-dependent sumoylation of HMGS-1 is the first reported case of well-characterized, regulated sumoylation with age. Presumably, age-dependent SUMO conjugation is a widespread mechanism controlling many metabolic and signaling networks during aging.

In contrast to the still uncharacterized role sumoylation plays during aging, the involvement of the ubiquitin–proteasome pathways is well established (41, 42). In *C. elegans* for example, proteasomal E3 ligase activity regulates lifespan (43), and elevated levels of proteasomal protein RPN-6 mediate somatic lifespan extension (44). This demonstrates how changes of the activity of the protein degradation machinery may consequently affect the lifespan of the organism. By their

nature, MS analyses (Fig. 4*B* and Fig. S8) are not tissue specific and represent the sum of interactors in the whole organism. As with ULP-4 (Fig. 1), it is likely that a spatiotemporal activity of specific interactors dictates the level HMGS-1 ubiquitination and activity in a tissue and age-specific manner. The cross-talk between the ubiquitin–proteasome and SUMO pathways may serve as a central mode of posttranslational modification. For example, substrate sumoylation triggers ubiquitination and protein degradation via the activity of SUMO-targeted ubiquitin E3 ligases (e.g., ref. 45). Likewise, HMGS-1 sumoylation at old age may lead to the binding of SUMO-dependent ubiquitin E3 ligases and protein degradation.

One fundamental characteristic of metabolism is its gross dependency and effect on the organism's life cycle. In many cases, metabolism is modulated and even rewired as the organism develops, ages, and copes with environmental and physiological stress. For example, an expression analysis of the *C. elegans* stress-resistant dauer larvae identified a switch from oxygenic respiration to anaerobic fermentation (46, 47). Even within the same organism, different tissues exhibit gross variability in metabolic profile. A comparison among 10 human tissues revealed that posttranscriptional regulation plays a central role in shaping tissue-specific metabolic profiles (48). Due to its vital role in cellular growth, differentiation, and basic activities such as cellular respiration, the mevalonate pathway is probably highly regulated during the life cycle of the organism. In humans, an age-dependent decrease in ubiquinone levels (49) and changes in cholesterol homeostasis (50) suggest that the pathway's activity changes with age. The dynamic regulation of HMGR1 by cholesterol and cholesterol-related metabolites probably cannot account for the more long-term control required during the organism's life cycle (36). Notably, large-scale proteomic studies reveal that almost every enzyme in the mevalonate pathway is subjected to ubiquitination (7). This suggests that ubiquitin-dependent degradation by the proteasome may play a role at many rate-limiting points of the pathway. So far, however, only one modified enzyme, squalene monooxygenase, has been investigated in detail (51, 52). The fact that HMGS-1/HMGCS1 activity allows substrates to enter the mevalonate pathway places its regulation as an effective control of flux from the pathway's starting point. Consistent with this notion, the level of HMGCS-1 transcription is highly controlled by the sterol-responding transcription factor SREBP (6) and by mutant p53 (4). Our findings highlight a HMGS-1 posttranslational modification network as an important regulatory mechanism for controlling the mevalonate pathway in *C. elegans*. Conservation of this network in the sterol-producing yeast *S. cerevisiae* (Fig. 4*C*) as well as the sumoylation of human HMGCS1 in vitro (Fig. 2*C*) suggests that this evolutionarily conserved mechanism may play a similar role in humans. Based on these data, we hypothesize that regulated HMGCS1 sumoylation along with ubiquitin–proteasome degradation control HMGS-1 activity with age. Perturbation of this regulatory network may contribute to pathway overactivation in various diseases such as p53-driven tumorigenesis and age-dependent loss of cholesterol homeostasis. This conserved molecular circuit could serve as a handle for targeting the mevalonate pathway in future therapeutics.

Methods

Yeast Two-Hybrid Screen. Yeast two-hybrid screens were performed by mating as previously described (53). Four distinct regions of *ulp-4* were used as bait: FL-ULP-4 (amino acids 1–382), N-ULP-4 (amino acids 1–110), Ex2-3ULP-4 (amino acids 58–145), and C-ULP-4 (amino acids 111–382). To avoid ULP-4-related toxicity, the predicted catalytic cysteine of the active site was mutated to serine (C743S) in constructs that bore the ULP-4 catalytic domain. To generate the *Gal4-DB::ulp-4* bait clones, the corresponding regions of the *ulp-4* coding sequence were PCR amplified from cDNA synthesized from mRNA of mixed-stage WT worms. A forward primer containing an AscI restriction site immediately upstream of the coding region was used with a reverse primer containing a stop codon followed by a NotI restriction site immediately downstream of the *ulp-4* coding region. These sites were used to clone each of the four fragments into the Gal4 DB vector pMB27, a modified version of pPC97 (54), which encodes a flexible linker (GGGG) upstream of the cloned ORF, and contains a polylinker that facilitates cloning using AscI and NotI restriction enzymes. Each of the *Gal4-DB::ulp-4* bait constructs were transformed into yeast strain Y8800 (55) and mated to a Gal4-AD-cDNA library (a generous gift from X. Xin and C. Boone, University of Toronto, Toronto) and a Gal4-AD-Fragment library containing fragments of 749 genes required for *C. elegans* early embryonic development (53). Both libraries were in yeast strain Y8930 (55). Candidate interactors were selected on Sc–Leu–Trp–His plates, and assayed on three additional plates: Sc–Leu–Trp–His + 2 mM 3-amino-1,2,4-triazole to gauge the strength of activation of the *HIS3* reporter gene, Sc–Leu–Trp–Ade to gauge the strength of activation of the *ADE2* reporter gene, and Sc–Leu–His + 1 μg/mL cycloheximide to identify yeast clones that are able to activate the *HIS3* reporter gene in the absence of an AD fusion protein as described (56). Clones that activate the *HIS3* reporter in the absence of a Gal4-AD interaction partner were eliminated. The identity of the remaining interactors was determined by PCR amplification from yeast cells and sequencing. As a final confirmation, we isolated the Gal4-AD plasmids, and transformed them into fresh Y8930 cells, which were mated with Gal4-DB-ULP-4 expressing Y8800 cells and again assayed for activation of the *HIS3* and *ADE2* reporter genes. Eight independent HMGS-1 clones were isolated from the Gal4-AD-cDNA library.

Detection of in Vivo Sumoylation. Worms were washed from starved plates and transferred to growing media (M9, 5 μg/mL cholesterol, 1 mM $MgSO_4$, and HB101 bacteria) and grown in liquid culture in one to three worms per μL density at 20 °C or 25 °C. For synchronized cultures beyond 3 d of adulthood, the *fer-15(b26)*II;*fem-1(hc17)*IV background was used. In this background, worms were grown at 25 °C until day 1 of adulthood and then were transferred to the desired temperature. Worms were harvested by three to four cycles of M9 washing and collection by spinning 1,160 × *g* for 2 min. When the M9 became clear, worms were divided into microcentrifuge tubes in aliquots of 300 mg compact worms. These aliquots were flash-frozen in liquid nitrogen and stored at −80 °C until analyzed. From this point forward, all steps were carried out at 4 °C unless otherwise stated. Worm pellets were resuspended in two volumes of cold worm lysis buffer (50 mM Tris·HCl, pH 7.4, 150 mM NaCl, 1 mM EDTA, 1% Triton X-100, 1 mM PMSF, 200 μM iodoacetamide, 1 minitablet of Roche protease inhibitor–EDTA/10 mL buffer, and 25 mM *N*-ethylmaleimide) prepared fresh and added to every tube just before sonication. Immediately after resuspension, worms were sonicated in five 10-s intervals with 50 s between each sonication interval. After sonication, each lysate was spun twice at 16,000 × *g* for 30 min and finally 16,000 × *g* for 5 min, transferring the supernatant to a new tube each time. After determination of protein concentration, 7 mg total protein from each lysate was diluted in 800 μL lysis buffer. For the IP, FLAG beads (Sigma; A2220) were thawed on ice, and 20 μL compact beads were used for every 300 μL compact worms. Lysate was placed on a roller overnight; then beads were pelleted by centrifugation at 685 × *g* and washed three times in lysis buffer. Next, protein was eluted from the beads by adding 100 μL 150 ng/μL 3×FLAG elution peptide in FLAG washing buffer. Samples were incubated for 30 min before the supernatants were transferred to a new microcentrifuge tube and 900 μL RIPA added to each tube. Anti-GFP antibody (Roche) was added to the tubes before incubating for 1 h. Next, protein-G beads were added and tubes were gently rolled for 7 h at 4 °C. As a final step, the beads were washed three times in FLAG washing buffer and sample buffer was added directly to the bead pellet.

Sumoylation Prediction and in Vitro Sumoylation Assays. Potential sumoylation sites were identified by integrating the predictions of three sumoylation prediction programs: SUMOplot (57), SUMOsp2.0 (58), and SUMO-RF. Lysine-to-arginine mutagenesis of candidate sites was done using Agilent technologies Quick Change site Directed Mutagenesis kit. WT and mutant HMGS-1 proteins were cloned into pET28B and transformed into BL-21 (DE3). Colonies were grown over 1 d at 37 °C, and protein expression was induced by 1 mM isopropyl β-D-1-thiogalactopyranoside (IPTG) overnight at 20 °C. Proteins were purified using standard techniques and were subjected to buffer exchange using Amicon centrifugal filters MWCO 10 kDa. After protein determination, 8 ng protein were used per sumoylation reaction preformed according to the manufacture's protocol. In vitro sumoylation reactions took place at 37 °C with an optimal incubation time of 30 min.

MS Analyses. ***IP.*** Worms were lysed in lysis buffer (1% Triton, 50 mM Tris pH 7.4, 150 mL NaCl, 1 mM EDTA, 250 μM iodoacetamide, 25 mM *N*-ethylmaleimide, 1 mM PMSF, 10 μM bortezomib, and 1 tablet of Roche complete protease inhibitor) by sonication using parameters similar to the in vivo sumoylation assays. Cell lysates were cleared by centrifugation for 30 min at 25,000 × *g* in an Eppendorf centrifuge (5417R), and supernatants were transferred to a new tube to repeat the centrifugation. For each IP, 50 μL FLAG beads were washed twice with 1 mL lysis buffer. Clear cell lysate was incubated with FLAG beads at 4 °C for 1 h. Beads were washed with 1 mL lysis buffer three times and 100 mM Tris buffer (pH 8.5) twice. Proteins were eluted with 10 M urea in 100 mM Tris buffer (pH 8.5) by incubating at 37 °C for 15 min.

In-solution tryptic digest followed by nano-liquid chromatography–tandem mass spectrometry analysis. Eluted proteins (100 μL) were diluted with 25 μL 100 mM Tris buffer (pH 8.5), reduced with 1 μL 0.5 M tris (2-carboxyethyl) phosphine hydrochloride (Thermo Fisher Scientific) for 20 min at 37 °C, alkylated with 3 μL 0.5 M chloroacetamide (Fisher) for 15 min at 37 °C, and digested with 2 μL 100 ng/μL Lysyl endopeptidase (Wako Chemicals; Lys-C) for 4 h at 37 °C. Samples were diluted to a final concentration of 2 M urea by adding 375 μL 100 mM Tris·HCl pH 8.5 and digested with 3 μL 100 ng/μL trypsin (Thermo Fisher Scientific) with 5 μL 100mM $CaCl_2$ for 18 h at 37 °C. After desalting with Pierce C18 Tip (Thermo Fisher Scientific), peptides were eluted with 200 μL 75% (vol/vol) acetonitrile (CAN) 0.1% TFA. Solvent was removed using a SpeedVac. Dried samples were acidified by 0.2% formic acid and loaded onto an Easy Nano-LC Q-Exactive Orbitrap (Thermo Fisher Scientific). Peptides were loaded onto to a trap column [PepMap 100 C18, 3 μm, 75 μm × 2 cm, nanoViper (Thermo Fisher Scientific)] and separated with an Easy-Spray column [PepMap C18, 3 μm 100 Å, 75 μm × 15 cm (Thermo Fisher Scientific, ES800) with a 2–30% (vol/vol) gradient (A: 0.1% formic acid [FA] in water; B: 0.1% FA in 100% CAN)] at 300 nL/min for 60 min followed by 30% (vol/vol) B to 100% B for 5 min and incubated at 100% B for 10 min.

The Q-Exactive acquisition method was created in data-dependent mode with one precursor scan in the Orbitrap, followed by fragmentation of the 15 most abundant peaks. Resolution of the precursor scan was set to 70,000, automatic gain control target 3e6, maximum injection time 100 ms, scanning from 350 to 2,000 *m/z*. The MS2 resolution was 17,500, the AGC target 5e4, the isolation window was 2.0 *m/z*, the fixed first mass 100.0 *m/z*, the normalized collision energy was 25, the underfill ratio was 0.1%, the charge exclusion was unassigned 1, peptide match was preferred, the exclude isotope option was on, and the dynamic exclusion was 30.0 s.

The peak list generating software used was Proteome Discoverer Software 1.4.1.14 (Thermo Fisher Scientific). The outline of the method used in the spectrum selector mode of the Proteome Discoverer software were all set to default settings to generate tandem MS spectra. The precursor charge state (high/low), retention time, minimum peak count, and total intensity threshold value were all set to default settings. The maximum and minimum precursor mass settings were 5,000 and 350 Da, respectively. The *C. elegans* Fasta file (canonical and isoform) was downloaded from UniProt (www.uniprot.org).

The Sequest HT search parameters included in this study were two missed cleavages allowed, fully tryptic peptides only, minimum peptide length of 6, maximum peptide length of 144, fixed modification of carbamidomethyl cysteine (+57.021 Da), dynamic modifications of oxidized methionine (+15.995Da), and N-terminal acetylation (+42.011Da). The precursor ion mass tolerance was 10 ppm and fragment mass tolerance was 0.05 Da. The input data maximum delta was Cn 0.05. The decoy database search was applied with strict false discovery rates (FDR) of 0.01 and relaxed FDR of 0.05, where the validation was based on *q* value.

Alignment of protein sequences and structures. The European Bioinformatics Institute (www.ebi.ac.uk) ClustalW multiple sequence alignment server (www.ebi.ac.uk/Tools/msa/clustalw2) was used to align all protein sequences with the default setting. Sequences were further annotated using Jalview 2.8 software (59). Human HMGCS1 modifications are based on data available from PhosphoSitePlus (www.phosphosite.org/homeAction.do). The Phyre server (60) was used for the search of proteins with an HMGS-1–related structure in the Protein Data Bank (www.rcsb.org/pdb/home/home.do) using default parameters. For the structural alignment of HMSG-1 and HMGCS1, we used PyMOL 1.3 software [The PyMOL Molecular Graphics System, Version 1.3 (Schrödinger); www.pymol.org].

Phylogenetic analysis of* C. elegans *ULPs and other Ulp/SENP family members. Protein sequences of Ulp/SENP were obtained by psi-BLAST search using National Center for Biotechnology Information Entrez nonredundant database (www.ncbi.nlm.nih.gov/refseq) or directly from genome sequencing projects. Two hundred fifty sequences from 75 organisms representing the 4 kingdoms of eukarya were aligned using multiple sequence comparison in the Log-Expectation program (61). Bootstrapping and determination of test estimate of maximum-likelihood tree topology were conducted with Rapid bootstrapping algorithm from RaxML Version 8.0.9 under the GTR+I model running on the CIPRES portal (62). Consensus tree images were generated using FigTree (www.molecularevolution.org/software/phylogenetics/figtree), and the tree images then manipulated using Adobe Photoshop software.

C. elegans *genetics.* Worm strains were cultured as in ref. 63. All integrated strains were out-crossed at least four times before experiments. The tm33688 *ulp-4* deletion was out-crossed at least seven times.

The strains used in this study were as follows:

PS6355: *ulp-4 (tm3688)/mIn1 [mIs14 dpy-10(e128)] II*

PS6366: *ulp-4 (tm3688)/mIn1 [mIs14 dpy-10(e128)] II; tvIs92 [ulp-4p::ulp-4::GFP]*

PS6709: *ulp-4 (tm3688)/mIn1 [mIs14 dpy-10(e128)] II; syIs261 [HMGS-1::GFP 1 ng/μL + pha-1 50 ng/μL + myo-2::mRFP 5 ng/μL]*

CF152: *fer-15(b26) II; fem-1(hc17) IV*

NX349: *fer-15(b26) II; fem-1(hc17) IV; syIa261 [HMGS-1::GFP 1 ng/μL + pha-1 50 ng/μL + myo-2::mRFP 5 ng/μL]; him-5(e1490) V*

PS6309: *syIs268 [myo-3p::TOM20::mRFP (50 μg/μL) + unc-119 (50 ng/μL)] V, tvIs92[ulp-4p::ulp-4::gfp; rol-6]*

NX92: *tvIs92[ulp-4p::ulp-4::gfp; rol-6]*

PS6332: *tvIs92 [ulp-4p::ulp-4::gfp], ljEx446 [pclh-3::mcherry (75 ng/μL), pRF4 (75 ng/μL]*

ulp-4 *molecular analysis and constructs.* The tm3668 deletion in the *ulp-4* locus was characterized by PCR of genomic DNA. For analysis of *ulp-4* transcripts in a *tm3688* background, total mRNA was purified from tm3668 homozygotes, heterozygotes, and WT worms. The mRNA was subjected to RT-PCR amplification with *ulp-4* specific primers. To generate *ulp-4* constructs, *ulp-4* DNA was amplified using DNA Expand Taq (Roche) or PfuUltra (Agilent Technologies), cloned into relevant plasmids, and sequenced. Injection, handling, and characterization of transgenic strains were done according to standard procedures.

HMGS-1/HMGCS1 constructs and worm strains. HMGS-1 cDNA was amplified from an open-biosystem RNAi library and cloned into pET28B plasmid for bacterial expression and in vitro sumoylation. The QuikChange site-directed mutagenesis technique (Agilent Technologies) was used for human HMGCS1 mutagenesis. For HMGCS1 cloning, total mRNA from human GM12878 cells (pre–B-cell lymphoblastoid) was amplified with *hmgcs1*-specific primers and cloned to the pET28B plasmid. To follow the expression pattern and sumoylation state of HMGS-1, worms were injected with a fosmid that harbors a tagged version of HMSG-1. This fosmid, which was obtained from the TransgeneOme project, had HMGS-1 followed by 2×TY, GFP, and 3×FLAG tags. The GFP tag was used for expression analysis, whereas the GFP and FLAG tags were used for biochemical analyses. Because of toxicity, the fosmid was injected at a final concentration of 1 ng/μL.

RNAi. RNAi knockdown was performed according to ref. 64 with minor modifications. Relevant RNAi clones were sequenced to verify clone identity. To induce RNAi in liquid cultures, worms were incubated with the RNAi expression bacteria of interest in the presence of 1 mM IPTG and 25 μg/mL carbenicillin.

Microscopy. ***Light microscopy.*** Larvae and adults were anesthetized with 10 mM levamisole, mounted on 2% (vol/vol) agar slides, and stored in a humid box until use. Images were captured using a Zeiss AxioImager M1 microscope and Axiovision software. Images for intensity comparison were taken with the same imaging parameters.

Confocal and superresolution microscopy. Embryos were harvested from gravid adults and mounted on a 2% (vol/vol) agar pad, covered with a 50 μL M9 drop and a small coverslip. Larvae and adults were immobilized on slides by using either levamisole anesthetics or the dry agar slide technique described in ref. 65. Images were captured using a Ziess LSM 510 confocal microscope. For superresolution analysis, worms were immobilized on dry agar slides and visualized using a Leica TCS sp5 II superresolution microscope (stimulated emission depletion). After acquisition, images were deconvoluted using the built-in deconvolution algorithms in the Leica LAS-AF software. The point spread function was generated with a 2D Lorentz function with the dull-width half-maximum set to 150 nm (as calculated on the image using the signal energy algorithm; regularization parameter of 0.1). For each stage or condition, *n* (number of animals) ≥ 15.

Oil-O-Red staining and measurement of total fat. The Oil-O-Red (Sigma; O9755) staining method was followed (66) with minor modifications.

TMRE staining. TMRE powder (Molecular Probes; T669) was dissolved in DMSO to make a 1-mM stock solution. This stock was further diluted 100× in M9 and used to stain worms for 30 min in microcentrifuge tubes in the dark. Then, worms were washed two to three times in M9 and mounted on dry agar slides. Because TMRE signal bleaches quickly samples were visualized using confocal microscopy.

Oxygen consumption measurements. The oxygen consumption rate was measured in a Seahorse Biosciences Extracellular Flux Analyzer (model XF96) using a protocol adapted from ref. 67. One-day-old worms of the indicated genotype were washed in M9 medium (to remove bacteria) and placed on bacteria-free nematode growth medium (NGM) agar plates. Ten worms were then manually transferred to each well in an XF96 measurement plate loaded with M9. Worms were allowed to settle to the bottom of the well, and oxygen consumption was measured four times per well. At least three different wells were measured for each condition or treatment.

Pharyngeal pumping and swimming measurements. To measure pharyngeal pumping, plates of worms were placed in a high-magnification stereomicroscope. Pharyngeal pumping was captured in 1-min movies of individual worms at 30 frames per s. These movies were opened in Image J and played at 8 frames per s. Pharyngeal pumping in 450 frames (15 s) was counted manually. To measure worm swimming, a single worm was placed in a drop of 40 μL M9 on an NGM plate using an eyelash hair. After 10 min, the swimming worm was captured in a movie as above. Analysis was done as above but the number of body turns was counted in 30 s. A standard body turn was defined as the complete change in direction of the bending at the midbody.

ACKNOWLEDGMENTS. We thank Shohei Mitani for a knockout allele, Ann Wang for the *ulp-4* RNAi in the *ulp-4::gfp* experiments, Adam Kolawa and Kevin Yu for their help with worm functional assays, Robyn Branicky and William Schafer for sharing the *clh-3*::mCherry worms, Brian Williams for total human RNA, David Chan for use of his Seahorse oxygen consumption analyzer, Domenico Fasci for his help with in vitro sumoylation assays, and Jennifer Watt for fat measurements. We also thank WormBase and the Caenorhabditis Genetics Center for *C. elegans* genetic annotation and strains. The Henry L. Guenther Foundation supported the Q-Exactive mass spectrometer. This research was supported by the Howard Hughes Medical Institute (of which P.W.S. is an Investigator), the Israel Cancer Research Fund PG -11-3086 (to L.B.), and Israel Science Foundation Grant ISF 1617/11 (to L.B.). A.T. was supported by the Ori Foundation-In Memory of Ori Levi, the Israeli Mitochondrial Disease Foundation (www.orifund.org). T.-F.C. is a member of University of California, Los Angeles's Jonsson Comprehensive Cancer Center. P.M. is supported by a Baxter Senior Postdoctoral Fellowship.

1. Brown MS, Goldstein JL (1980) Multivalent feedback regulation of HMG CoA reductase, a control mechanism coordinating isoprenoid synthesis and cell growth. *J Lipid Res* 21(5):505–517.
2. Zhang FL, Casey PJ (1996) Protein prenylation: Molecular mechanisms and functional consequences. *Annu Rev Biochem* 65:241–269.
3. Rauthan M, Pilon M (2011) The mevalonate pathway in C. elegans. *Lipids Health Dis* 10:243.
4. Freed-Pastor WA, et al. (2012) Mutant p53 disrupts mammary tissue architecture via the mevalonate pathway. *Cell* 148(1-2):244–258.
5. DeBose-Boyd RA (2008) Feedback regulation of cholesterol synthesis: Sterol-accelerated ubiquitination and degradation of HMG CoA reductase. *Cell Res* 18(6):609–621.
6. Goldstein JL, Brown MS (1990) Regulation of the mevalonate pathway. *Nature* 343(6257):425–430.
7. Sharpe LJ, Brown AJ (2013) Controlling cholesterol synthesis beyond 3-hydroxy-3-methylglutaryl-CoA reductase (HMGCR). *J Biol Chem* 288(26):18707–18715.
8. Smith JR, Osborne TF, Brown MS, Goldstein JL, Gil G (1988) Multiple sterol regulatory elements in promoter for hamster 3-hydroxy-3-methylglutaryl-coenzyme A synthase. *J Biol Chem* 263(34):18480–18487.
9. Van Hoof D, et al. (2009) Phosphorylation dynamics during early differentiation of human embryonic stem cells. *Cell Stem Cell* 5(2):214–226.
10. Choudhary C, et al. (2009) Lysine acetylation targets protein complexes and co-regulates major cellular functions. *Science* 325(5942):834–840.
11. Kim W, et al. (2011) Systematic and quantitative assessment of the ubiquitin-modified proteome. *Mol Cell* 44(2):325–340.
12. Wagner SA, et al. (2011) A proteome-wide, quantitative survey of in vivo ubiquitylation sites reveals widespread regulatory roles. *Mol Cell Proteomics* 10(10):M111.013284.
13. Wagner SA, et al. (2012) Proteomic analyses reveal divergent ubiquitylation site patterns in murine tissues. *Mol Cell Proteomics* 11(12):1578–1585.
14. Flotho A, Melchior F (2013) Sumoylation: A regulatory protein modification in health and disease. *Annu Rev Biochem* 82:357–385.
15. Gareau JR, Lima CD (2010) The SUMO pathway: Emerging mechanisms that shape specificity, conjugation and recognition. *Nat Rev Mol Cell Biol* 11(12):861–871.
16. Braschi E, Zunino R, McBride HM (2009) MAPL is a new mitochondrial SUMO E3 ligase that regulates mitochondrial fission. *EMBO Rep* 10(7):748–754.
17. Kaminsky R, et al. (2009) SUMO regulates the assembly and function of a cytoplasmic intermediate filament protein in C. elegans. *Dev Cell* 17(5):724–735.
18. Mukhopadhyay D, Dasso M (2007) Modification in reverse: The SUMO proteases. *Trends Biochem Sci* 32(6):286–295.
19. Yeh ET (2009) SUMOylation and de-SUMOylation: Wrestling with life's processes. *J Biol Chem* 284(13):8223–8227.
20. Li SJ, Hochstrasser M (2003) The Ulp1 SUMO isopeptidase: Distinct domains required for viability, nuclear envelope localization, and substrate specificity. *J Cell Biol* 160(7): 1069–1081.
21. Zunino R, Braschi E, Xu L, McBride HM (2009) Translocation of SenP5 from the nucleoli to the mitochondria modulates DRP1-dependent fission during mitosis. *J Biol Chem* 284(26):17783–17795.
22. Dou H, Huang C, Singh M, Carpenter PB, Yeh ETH (2010) Regulation of DNA repair through deSUMOylation and SUMOylation of replication protein A complex. *Mol Cell* 39(3):333–345.
23. Hegardt FG (1999) Mitochondrial 3-hydroxy-3-methylglutaryl-CoA synthase: A control enzyme in ketogenesis. *Biochem J* 338(Pt 3):569–582.
24. Weltzien FA, Hemre GI, Evjemo JO, Olsen Y, Fyhn HJ (2000) Beta-hydroxybutyrate in developing nauplii of brine shrimp (Artemia franciscana K.) under feeding and non-feeding conditions. *Comp Biochem Physiol B Biochem Mol Biol* 125(1):63–69.
25. Beis A, Zammit VA, Newsholme EA (1980) Activities of 3-hydroxybutyrate dehydrogenase, 3-oxoacid CoA-transferase and acetoacetyl-CoA thiolase in relation to ketone-body utilisation in muscles from vertebrates and invertebrates. *Eur J Biochem* 104(1):209–215.
26. Shi Z, Ruvkun G (2012) The mevalonate pathway regulates microRNA activity in Caenorhabditis elegans. *Proc Natl Acad Sci USA* 109(12):4568–4573.
27. Liu Y, Samuel BS, Breen PC, Ruvkun G (2014) Caenorhabditis elegans pathways that surveil and defend mitochondria. *Nature* 508(7496):406–410.
28. Kim MJ, Chia IV, Costantini F (2008) SUMOylation target sites at the C terminus protect Axin from ubiquitination and confer protein stability. *FASEB J* 22(11):3785–3794.
29. Hickey CM, Wilson NR, Hochstrasser M (2012) Function and regulation of SUMO proteases. *Nat Rev Mol Cell Biol* 13(12):755–766.
30. Dillin A, et al. (2002) Rates of behavior and aging specified by mitochondrial function during development. *Science* 298(5602):2398–2401.
31. Husnjak K, et al. (2008) Proteasome subunit Rpn13 is a novel ubiquitin receptor. *Nature* 453(7194):481–488.
32. Stark C, et al. (2006) BioGRID: A general repository for interaction datasets. *Nucleic Acids Res* 34(Database issue):D535–D539.
33. Hannich JT, et al. (2005) Defining the SUMO-modified proteome by multiple approaches in Saccharomyces cerevisiae. *J Biol Chem* 280(6):4102–4110.
34. Peng J, et al. (2003) A proteomics approach to understanding protein ubiquitination. *Nat Biotechnol* 21(8):921–926.
35. Sung MK, et al. (2013) Genome-wide bimolecular fluorescence complementation analysis of SUMO interactome in yeast. *Genome Res* 23(4):736–746.
36. Sever N, Yang T, Brown MS, Goldstein JL, DeBose-Boyd RA (2003) Accelerated degradation of HMG CoA reductase mediated by binding of insig-1 to its sterol-sensing domain. *Mol Cell* 11(1):25–33.
37. Broday L, et al. (2004) The small ubiquitin-like modifier (SUMO) is required for gonadal and uterine-vulval morphogenesis in Caenorhabditis elegans. *Genes Dev* 18(19): 2380–2391.
38. Bolender N, Sickmann A, Wagner R, Meisinger C, Pfanner N (2008) Multiple pathways for sorting mitochondrial precursor proteins. *EMBO Rep* 9(1):42–49.
39. Zhang L, Li F, Dimayuga E, Craddock J, Keller JN (2007) Effects of aging and dietary restriction on ubiquitination, sumoylation, and the proteasome in the spleen. *FEBS Lett* 581(28):5543–5547.
40. Nisticò R, et al. (2014) Age-related changes of protein SUMOylation balance in the AβPP Tg2576 mouse model of Alzheimer's disease. *Front Pharmacol* 5:63.
41. Löw P (2011) The role of ubiquitin-proteasome system in ageing. *Gen Comp Endocrinol* 172(1):39–43.
42. Kevei É, Hoppe T (2014) Ubiquitin sets the timer: Impacts on aging and longevity. *Nat Struct Mol Biol* 21(4):290–292.
43. Ghazi A, Henis-Korenblit S, Kenyon C (2007) Regulation of Caenorhabditis elegans lifespan by a proteasomal E3 ligase complex. *Proc Natl Acad Sci USA* 104(14): 5947–5952.
44. Vilchez D, et al. (2012) RPN-6 determines C. elegans longevity under proteotoxic stress conditions. *Nature* 489(7415):263–268.
45. Tatham MH, et al. (2008) RNF4 is a poly-SUMO-specific E3 ubiquitin ligase required for arsenic-induced PML degradation. *Nat Cell Biol* 10(5):538–546.
46. Burnell AM, Houthoofd K, O'Hanlon K, Vanfleteren JR (2005) Alternate metabolism during the dauer stage of the nematode Caenorhabditis elegans. *Exp Gerontol* 40(11):850–856.
47. Mádi A, et al. (2008) Mass spectrometric proteome analysis suggests anaerobic shift in metabolism of Dauer larvae of Caenorhabditis elegans. *Biochim Biophys Acta* 1784(11):1763–1770.
48. Shlomi T, Cabili MN, Herrgård MJ, Palsson BO, Ruppin E (2008) Network-based prediction of human tissue-specific metabolism. *Nat Biotechnol* 26(9):1003–1010.
49. Bentinger M, Tekle M, Dallner G (2010) Coenzyme Q—biosynthesis and functions. *Biochem Biophys Res Commun* 396(1):74–79.
50. Martin M, Dotti CG, Ledesma MD (2010) Brain cholesterol in normal and pathological aging. *Biochim Biophys Acta* 1801(8):934–944.

51. Foresti O, Ruggiano A, Hannibal-Bach HK, Ejsing CS, Carvalho P (2013) Sterol homeostasis requires regulated degradation of squalene monooxygenase by the ubiquitin ligase Doa10/Teb4. *Elife (Cambridge)* 2:e00953.
52. Zelcer N, et al. (2014) The E3 ubiquitin ligase MARCH6 degrades squalene monooxygenase and affects 3-hydroxy-3-methyl-glutaryl coenzyme A reductase and the cholesterol synthesis pathway. *Mol Cell Biol* 34(7):1262–1270.
53. Boxem M, et al. (2008) A protein domain-based interactome network for C. elegans early embryogenesis. *Cell* 134(3):534–545.
54. Vidal M, Brachmann RK, Fattaey A, Harlow E, Boeke JD (1996) Reverse two-hybrid and one-hybrid systems to detect dissociation of protein-protein and DNA-protein interactions. *Proc Natl Acad Sci USA* 93(19):10315–10320.
55. Yu H, et al. (2008) High-quality binary protein interaction map of the yeast interactome network. *Science* 322(5898):104–110.
56. Vidalain PO, Boxem M, Ge H, Li S, Vidal M (2004) Increasing specificity in high-throughput yeast two-hybrid experiments. *Methods* 32(4):363–370.
57. Xue Y, Zhou F, Fu C, Xu Y, Yao X (2006) SUMOsp: A web server for sumoylation site prediction. *Nucleic Acids Res* 34(Web Server issue):W254–257.
58. Ren J, et al. (2009) Systematic study of protein sumoylation: Development of a site-specific predictor of SUMOsp 2.0. *Proteomics* 9(12):3409–3412.
59. Waterhouse AM, Procter JB, Martin DM, Clamp M, Barton GJ (2009) Jalview Version 2—a multiple sequence alignment editor and analysis workbench. *Bioinformatics* 25(9):1189–1191.
60. Kelley LA, Sternberg MJ (2009) Protein structure prediction on the Web: A case study using the Phyre server. *Nat Protoc* 4(3):363–371.
61. Edgar RC (2004) MUSCLE: Multiple sequence alignment with high accuracy and high throughput. *Nucleic Acids Res* 32(5):1792–1797.
62. Stamatakis A, Hoover P, Rougemont J (2008) A rapid bootstrap algorithm for the RAxML Web servers. *Syst Biol* 57(5):758–771.
63. Brenner S (1974) The genetics of Caenorhabditis elegans. *Genetics* 77(1):71–94.
64. Timmons L, Court DL, Fire A (2001) Ingestion of bacterially expressed dsRNAs can produce specific and potent genetic interference in Caenorhabditis elegans. *Gene* 263(1-2):103–112.
65. Han SM, et al. (2012) Secreted VAPB/ALS8 major sperm protein domains modulate mitochondrial localization and morphology via growth cone guidance receptors. *Dev Cell* 22(2):348–362.
66. Yen K, et al. (2010) A comparative study of fat storage quantitation in nematode Caenorhabditis elegans using label and label-free methods. *PLoS ONE* 5(9):e12810.
67. Houtkooper RH, et al. (2013) Mitonuclear protein imbalance as a conserved longevity mechanism. *Nature* 497(7450):451–457.

Supporting Information

Sapir et al. 10.1073/pnas.1414748111

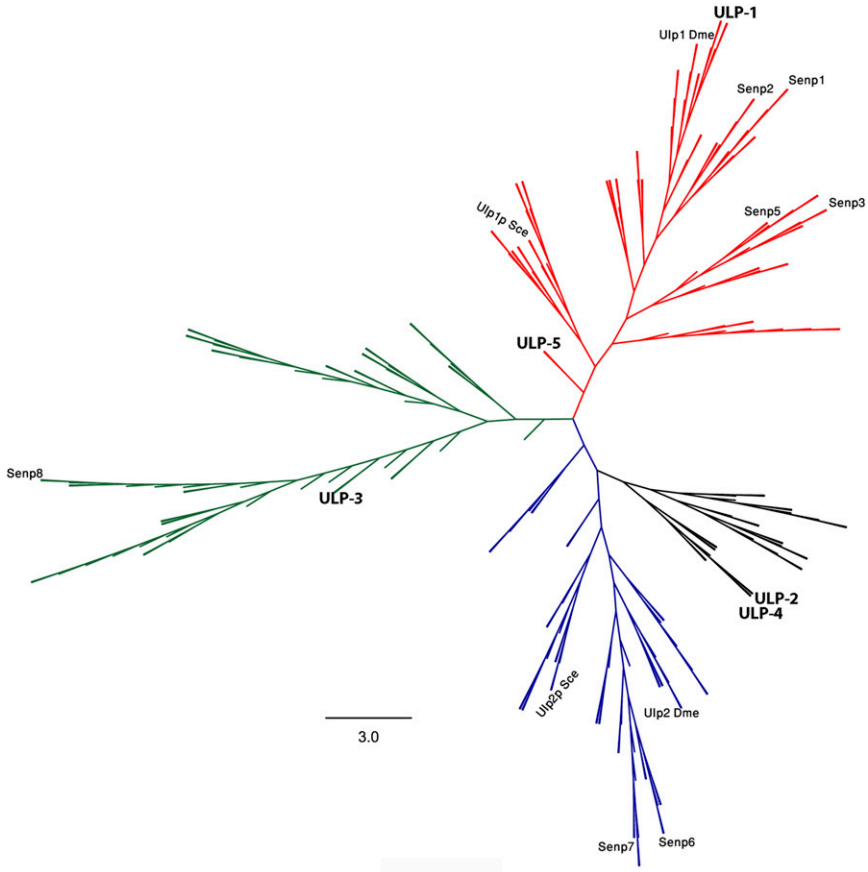

Fig. S1. Phylogenetic tree of *Caenorhabditis elegans* ULPs and other ULPs/SENPs. *C. elegans* ULPs are labeled in bold font. Colors represent different ULP/SENP families. Human SENPs 1–3; 5–8 are shown as well as ULPs of *Drosophila melanogaster* (Dme) and *Saccharomyces cerevisiae* (Sce). (Scale bar: branch length, which is expressed as the expected number of substitutions per site.)

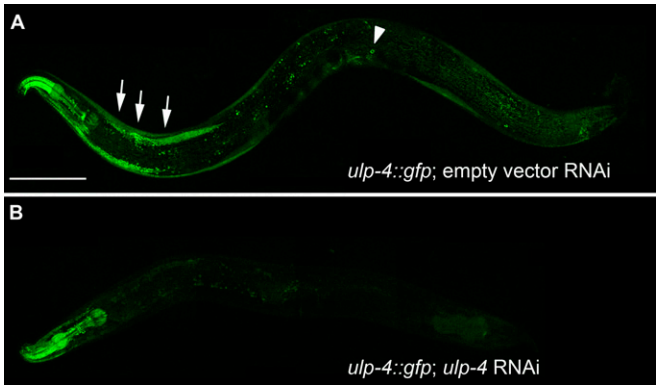

Fig. S2. *ulp-4*::gfp signal is reduced by *ulp-4* RNAi. We tested the activity of *ulp-4* RNAi on worms expressing *ulp-4p*::*ulp-4*::GFP. (*A*) The stereotypic expression pattern of *ulp-4*::GFP in day-1 adult hermaphrodites fed with empty vector RNAi. Hermaphroditic-specific neuron (HSN) expression (white arrowhead) and expression in head muscles (white arrows) are shown. (*B*) *ulp-4* RNAi activity resulted in the elimination of GFP signal from body wall muscle cells and HSN neurons. When the worms were treated with *ulp-4* RNAi for more than two generations, the signal was also reduced in pharyngeal cells. (Scale bar: 50 μm.)

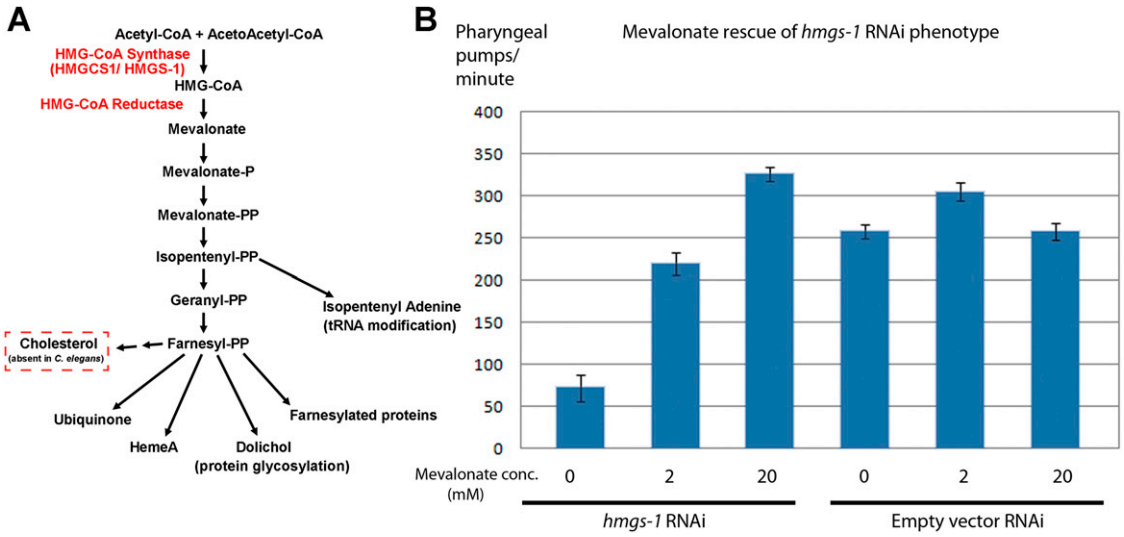

Fig. S3. *hmgs-1* knockdown is rescued by mevalonate supplementation. (*A*) A schematic representation of mevalonate pathway metabolism. Cholesterol production is absent in *C. elegans* but other branches of the pathway are conserved. (*B*) Worms fed with *hmgs-1* RNAi show a significant reduction in the level of pharyngeal pumping. This effect can be fully rescued by supplementation of 20 mM mevalonate indicating that *hmgs-1* knockdown phenotypes stem from impaired mevalonate pathway flux. 20mM mevalonate does not affect the pumping rate of WT worms; precluding a nonspecific rescue by mevalonate supplementation. Bars represent SEs. Number of worms, $n = 10$ WT worms in each condition.

A

Prediction method		SUMOplot			SUMOsp2			SUMO-RF	
C.elegans	Site	Sequence	Score	Site	Sequence	Score	Site	Sequence	Score
HMGS-1	291	GNGVDHKLDENDRA	0.52	408	FTETLQKREVFLRS	3.015	408	FTETLQKREVFLRS	77.11
	314	AQVWKEKTDPYLVF	0.5				314	AQVWKEKTDPYLVF	49.21
	408	FTETLQKREVFLRS	0.5						
	420	RSKEIPKSPSETSL	0.5						
Human									
HMGCS1	305	EAFGDVKLEDTYFD	0.93	105	KSVKTNL	2.853	305	EAFGDVKLEDTYFD	100
	55	IGLGQAKMGFCTDR	0.62	321	AFMKASS	2.265	206	DFYKPDM	61.84
	38	DQAELEKYDGVDAG	0.5	499	PAKKVPR	2.279			
	499	IPSPAKKVPRLPAT	0.37	305	GDVKLED	1.749			
	246	IHAQWQKEGNDKDF	0.33						
	315	FDRDVEKAFMKASS	0.15						
	251	QKEGNDKDFTLNDF	0.15						

B

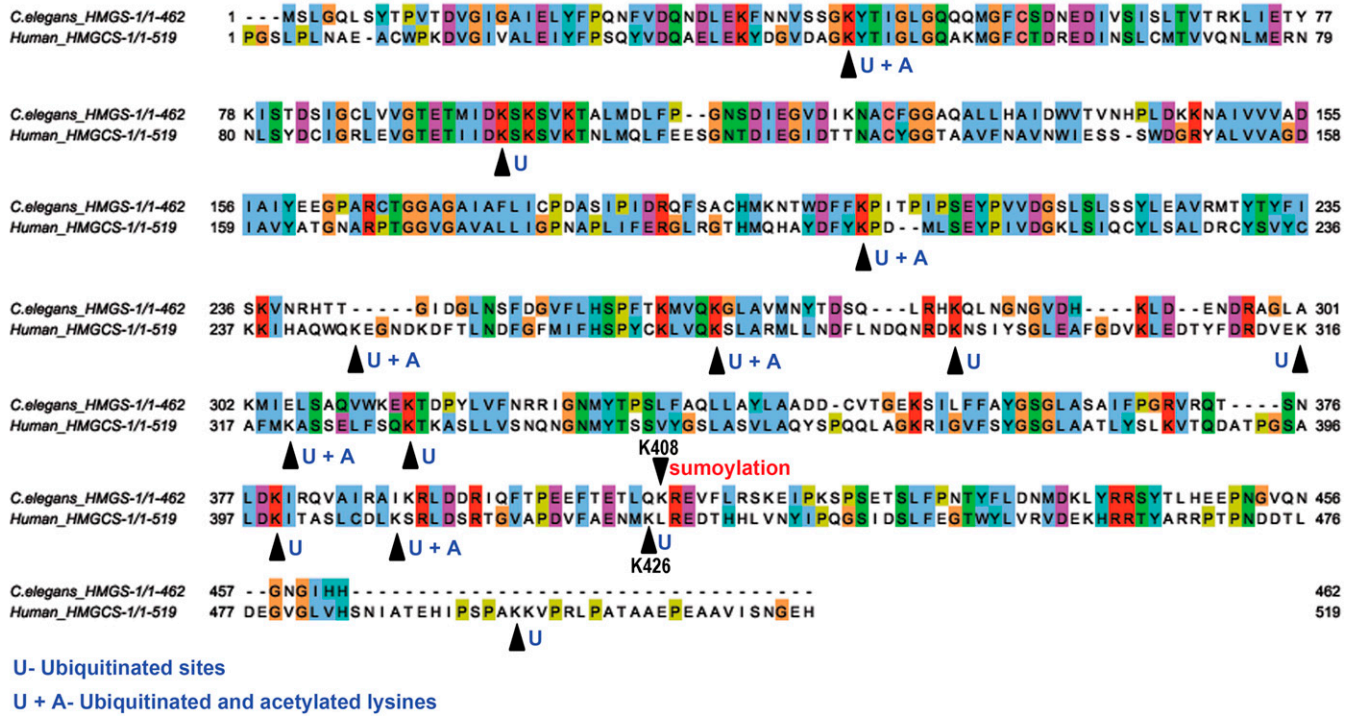

Fig. S4. A comparison between HMGS-1 and human HMG-CoA synthase 1 (HMGCS1) modifications. (*A*) Prediction of sumoylation sites in HMGS-1 and HMGCS1 proteins. Lysine (K) highlighted in red are the residues predicted to be sumoylated. (*B*) HMGCS1 undergoes ubiquitination and acetylation at multiple sites. Human HMGCS1 modifications are based on data available from PhosphoSitePlus (www.phosphosite.org/homeAction.do). Sequences were aligned using ClustalW (www.ebi.ac.uk/Tools/msa/clustalw2) and visualized using Jalview software (1).

1. Waterhouse AM, Procter JB, Martin DM, Clamp M, Barton GJ (2009) Jalview Version 2—a multiple sequence alignment editor and analysis workbench. *Bioinformatics* 25(9):1189–1191.

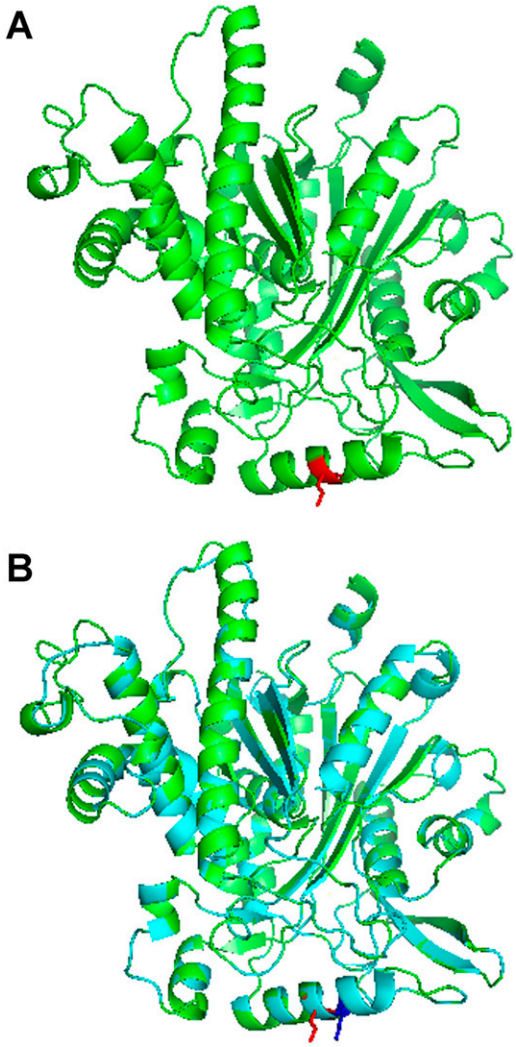

Fig. S5. A model of HMGS-1 structure and its alignment with human HMGCS1. (*A*) Predicted HMGS-1 3D structure based on a Protein Data Bank structural search (www.rcsb.org/pdb/home/home.do). HMGS-1 shares the same structure with the human proteins HMGCS2 (42%) and HMGCS1 (40%) with confidence of 100%. The sumoylated Lys408 is labeled in red. (*B*) Alignment between HMGS-1 and its functional human ortholog HMGCS1. On the HMGCS1 structure, K426 which is the closest to the sumoylated residue of HMGS-1 is labeled in blue. This residue was found to undergo ubiquitination in human HMGCS1. The Phyre server (1) was used to search for proteins with a HMGS-1–related structure.

1. Kelley LA, Sternberg MJ (2009) Protein structure prediction on the Web: A case study using the Phyre server. *Nat Protoc* 4(3):363–371.

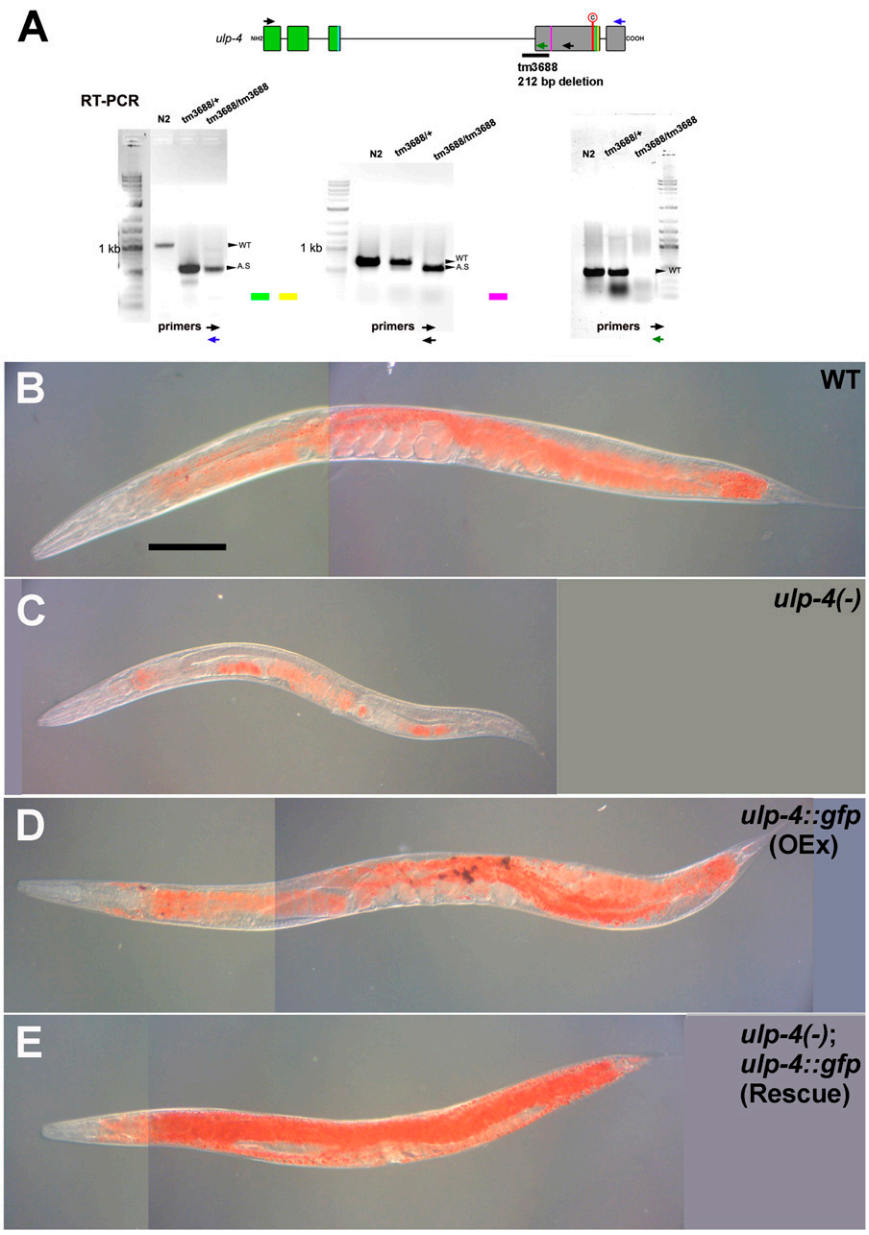

Fig. S6. Molecular characterization of the *ulp-4* locus and its requirement for normal fat homeostasis. (*A*) RT-PCR analyses of *tm3886* within the *ulp-4* locus. The *ulp-4* N-terminal region is in green (exons 1–3). This is followed by the C-terminal region (exons 4–5) that is labeled in gray. This region harbors the *ulp-4* catalytic domain (the conserved cysteine is labeled "©"). RT-PCR analyses revealed that in the strain homozygous for the tm3886 deletion, a truncated transcript still exists. Because the tm3886 deletion introduces a frame shift followed by a stop codon before the catalytic site, this transcript presumably does not code for a functional ULP-4 protein. (*B*–*E*) Worms' fat level was determined by Oil-O-Red staining. (*C*) *ulp-4*(tm3688) mutant worms have less fat than the WT control (*B*). (*D*) The level of fat is marginally increased in worms overexpressing *ulp-4::gfp*. (*E*) *ulp-4::gfp* construct partially rescues the fat loss of *ulp-4(-)* mutants, indicating that the *ulp-4::gfp* construct is functional. (Scale bar: 50 μm.)

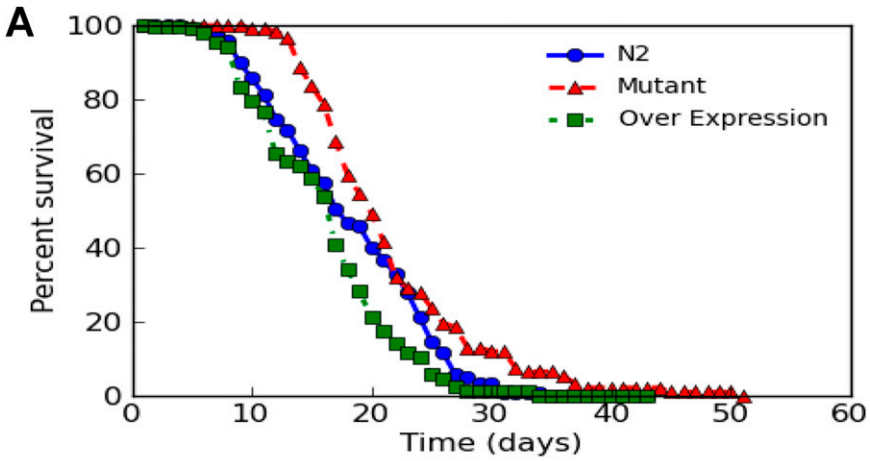

B

Mean/Median Lifespan

Name	No. of subjects	Days	Std. error	95% C.I.	25%	50%	75%	90%	100%	95% Median C.I.
		----------Restricted Mean----------			----------Age in days at % mortality----------					
N2	243	18.28	0.56	17.19~19.37	12	18	24	27	35	16~19
Mutant	152	21.78	0.69	20.44~23.13	17	20	25	32	51	19~21
Over Expression	202	16.26	0.57	15.13~17.38	12	17	20	25	34	15~17

C

Condition	Statistics		
	Chi^2	P-value	Bonferroni P-value
N2 *v.s.* **Mutant**	11.90	0.0006	0.0011
N2 *v.s.* **Over Expression**	7.08	0.0078	0.0156
Mutant *v.s.* **N2**	11.90	0.0006	0.0011
Mutant *v.s.* **Over Expression**	32.35	1.3e-08	2.6e-08
Over Expression *v.s.* **N2**	7.08	0.0078	0.0156
Over Expression *v.s.* **Mutant**	32.35	1.3e-08	2.6e-08

Fig. S7. Opposite effects of *ulp-4* loss and *ulp-4* overexpression (ulp-4::GFP) on *C. elegans* lifespan. (*A*) Lifespan analyses of WT, *ulp-4* mutants, and worms overexpressing *ulp-4* under its own promoter. (*B*) *ulp-4* mutants have a longer median and maximal lifespan than WT controls, whereas *ulp-4* overexpression exhibits an opposite effect. The effect of *ulp-4* on *C. elegans* lifespan is significant based on multiple statistical analyses. (*C*) All lifespan experiments were held at 20 °C on plates seeded with *Escherischia coli*, strain OP50, at the same time.

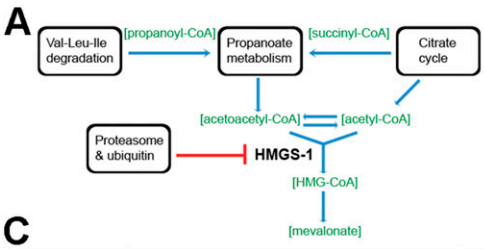

B

KEGG Pathway	Fold enrichment	P-value (Benjamini-corrected)	Number of genes
Ribosome	5.5	1.60E-48	73
Citrate cycle	3.1	0.001	16
VLI degradation	2.8	7.00E-04	19
Propanoate metabolism	2.8	0.014	13
Proteasome	2.4	2.00E-02	15

C

Accession	Description	Coverage (%)	# Unique Peptides	# PSMs	Fold Enrichment
P54871	Hydroxymethylglutaryl-CoA synthase, [HMCS_CAEEL]	55.41	14	107	>>16.8
Q19584	Ubiquitin fusion degradation protein 1 homolog, [UFD1_CAEEL]	48.83	9	46	>>16.8
Q95Y72	Probable 26S proteasome complex subunit dss-1, [DSS1_CAEEL]	23.17	1	1	>>16.8
Q95008	Proteasome subunit alpha type-5, [PSA5_CAEEL]	21.37	3	10	>>16.8
P91430	Ubiquitin-like modifier-activating enzyme 5, [UBA5_CAEEL]	15.27	5	7	>>16.8
Q04908	26S proteasome non-ATPase regulatory subunit 3, [PSMD3_CAEEL]	8.13	3	11	>>16.8
Q20938	Probable 26S proteasome regulatory subunit rpn-6.1, [PS11A_CAEEL]	7.08	2	7	>>16.8
Q966I8	Proteasome subunit beta type [Q966I8_CAEEL]	6.28	1	1	>>16.8
G5ED41	Cullin-associated NEDD8-dissociated protein 1, [CAND1_CAEEL]	3.85	3	4	>>16.8
Q09444	Probable ubiquitin carboxyl-terminal hydrolase, [UBH4_CAEEL]	2.49	1	2	>>16.8
O16368	Probable 26S protease regulatory subunit 4, [PRS4_CAEEL]	16.93	5	15	16.8
Q18787	26S protease regulatory subunit 7, [PRS7_CAEEL]	30.11	10	32	10.8
Q95XX0	Protein UBC-13 (Ubiquitin E2) [Q95XX0_CAEEL]	18.54	1	1	5.6
P46502	Probable 26S protease regulatory subunit 6B, [PRS6B_CAEEL]	24.15	7	30	5.1
P37165	Ubiquitin-like protein 1-40S ribosomal protein S27a, [RS27A_CAEEL]	23.31	2	49	5.0
P0CG71	Polyubiquitin-A, [UBIQ1_CAEEL]	44.63	3	44	4.2
O17071	Probable 26S protease regulatory subunit 10B, [PRS10_CAEEL]	28.82	9	48	3.8
P54811	Transitional endoplasmic reticulum ATPase homolog 1, Cdc48-1, [TERA1_CAEEL]	16.56	4	39	3.6
P54812	Transitional endoplasmic reticulum ATPase homolog 2, Cdc48-2, [TERA2_CAEEL]	10.25	1	28	3.1
O76577	26S proteasome non-ATPase regulatory subunit 14, [PSDE_CAEEL]	11.86	3	19	3.0
Q18231	Protein RPS-30, [Q18231_CAEEL]	8.46	2	13	2.9

Fig. S8. Proteomic analysis of HMGS-1 interactors. (*A*) A diagram of the metabolic network discovered by the survey of HMGS-1 interactors. This analysis suggests that acetyl-CoA and acetoacetyl-CoA synthesis is physically coupled to condensation by HMGS-1, presumably in a hand-off type of mechanism. (*B*) Statistics of the Kyoto Encyclopedia of Genes and Genomes (KEGG, www.genome.jp/kegg) components enriched in the immunoprecipitated fraction based on a KEGG analysis performed with the Database for Annotation, Visualization and Integrated Discovery (DAVID, http://david.abcc.ncifcrf.gov/home.jsp) (1). (*C*) The list of ubiquitin–proteasome-related proteins interacting with HMGS-1. HMGS-1 itself, labeled in red, was found as the most enriched protein in the immunoprecipitated fraction, demonstrating the potency of our assay. The list is comprised of fifteen proteins identified by Eukaryotic Orthologous Groups of proteins analysis (http://genome.jgi-psf.org/help/kogbrowser.jsf) and five proteins that were identified manually.

1. Huang DW, Sherman BT, Lempicki RA (2009) Bioinformatics enrichment tools: Paths toward the comprehensive functional analysis of large gene lists. *Nucleic Acids Res* 37(1):1–13.

```
SENP-6_Human/1-1112      1 --MAAGKSGGSAGEITFLEALARSESKRDGGFKNNWSFDHEEESEGDTDKDGT 51
ULP-4_C.elegans/1-382      ------------------------------------------------------
SENP-3_Human/1-574       1 MKETIQGTGSWGPEPPGPGIPPAYSSPRRERLRWPPPPKPRLKSGGGFGPDPG 53

SENP-6_Human/1-1112     52 NLLSVDEDEDSETSKGKKLNRRSEIVANSSGEFILKTYVRRNKSESFKTLKGN 104
ULP-4_C.elegans/1-382      ------------------------------------------------------
SENP-3_Human/1-574      54 -------SGTTVPARRLPVPRPSFDASASEEEEEEEEEEDEDEEEEVAAWRLP 99

SENP-6_Human/1-1112    105 PIGLNMLSNNKKLSENTQNTSLCSG-TVVHGRRFHHAHAQIPVVKTAAQSSLD 156
ULP-4_C.elegans/1-382      ------------------------------------------------------
SENP-3_Human/1-574     100 PRWSQLGTSQRPRPSRPTHRKTCSQRRRRAMRAFRMLLYSKSTSLTFHWKLWG 152

SENP-6_Human/1-1112    157 RKERKEYPPHVQKVEINPVRLSRLQGVERIMKKTEESESQVEPEIKRKVQQKR 209
ULP-4_C.elegans/1-382    1 ---------------------------------MEVSTSYCTPAVN-------13
SENP-3_Human/1-574     153 RHRGRRRGLAHPKNHLSPQQGGATPQVPSPCCRFDSPRGPPPPRLG-------198

SENP-6_Human/1-1112    210 HCSTYQPTPPLSPASKKCLTHLEDLQRNCRQAITLNESTGPLLRTSIHQNSGG 262
ULP-4_C.elegans/1-382   14 -------------------------FKYGSFQDSDVSMREDDLFRMGSYNSQG-41
SENP-3_Human/1-574     199 ----------------LLGALMAEDGVRGSPPVPSGPPMEEDGLRWTPKSPLDP 236

SENP-6_Human/1-1112    263 QKSQNTGLTTKKFYGNNVEKVPIDIIVNCDDSKHTYLQTNGKVILPGAKIPKI 315
ULP-4_C.elegans/1-382   42 -------------YYAD-----------------GTHLDG---------------51
SENP-3_Human/1-574     237 DSGLLSCTLPNGFGGQSGPEGERSLAPPDASILISNVCSIGDHVAQELFQGSD 289

SENP-6_Human/1-1112    316 TNLKERKTSLSDLNDPIILSSDDDDDNDRTNRRESISPQPADSACSSPAPSTG 368
ULP-4_C.elegans/1-382   52 -SIGEEDETSSGSNDQHMDFEEDDFDMESSMTEDLVDEDEEEE----------93
SENP-3_Human/1-574     290 LGMAEEAERPGEKAGQHSPLREEHVTCVQSILDEFLQTYGSLIP---------333

SENP-6_Human/1-1112    369 KVEAALNENTCRAERELRSIPEDSELNTVTLPRKARMKDQFGNSIINTPLKRR 421
ULP-4_C.elegans/1-382      ------------------------------------------------------
SENP-3_Human/1-574         ------------------------------------------------------

SENP-6_Human/1-1112    422 KVFSQEPPDALALSCQSSFDSVILNCRSIRVGTLFRLLIEPVIFCLDFIKIQL 474
ULP-4_C.elegans/1-382      ------------------------------------------------------
SENP-3_Human/1-574         ------------------------------------------------------L 334

SENP-6_Human/1-527     475 DEPDHDPVEIILNTSDLTKCEWCNVRKLPVVFLQAIPAVYQKLSIQLQMNKED 527
ULP-4_C.elegans/1-130   94 DEEDND----------------EWTNQKRTDNQNSVAYYAAMEMLRIRFPFQS--130
SENP-3_Human/1-385     335 STDEVVEKLEDIFQQEFSTPSRKGLVLQLIQSYQRMPGNAMVRGFRVAYKR--385
```

Fig. S9. ClustalW sequence alignment between *C. elegans* ULP-4 small ubiquitin-like modifier protease and human SENP3 and SENP6. Specific acidic residues are labeled in red, and acidic regions (rich in acidic residues) are underlined in blue. Acidic regions are not present in other human SENPs. The alignment was annotated using Jalview software (1).

1. Waterhouse AM, Procter JB, Martin DM, Clamp M, Barton GJ (2009) Jalview Version 2—a multiple sequence alignment editor and analysis workbench. *Bioinformatics* 25(9):1189–1191.

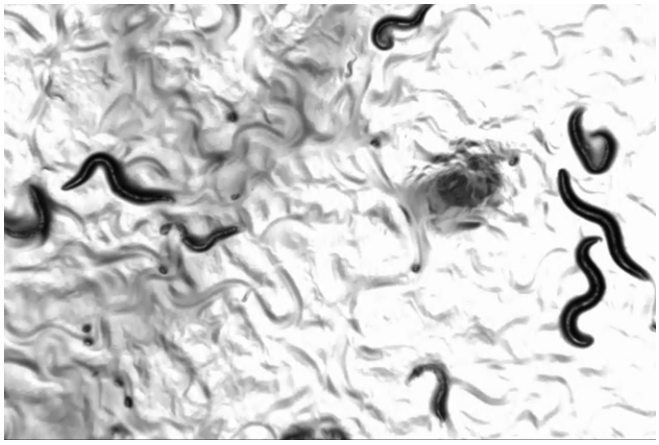

Movie S1. WT worms on *hmgs-1* RNAi. A movie of 30 frames per second showing day-1 adult WT worms grown from egg to adulthood on *hmgs-1* RNAi. Treatment with *hmgs-1* RNAi results in slow development, small body size, partial sterility, and severe worm paralysis.

Movie S1

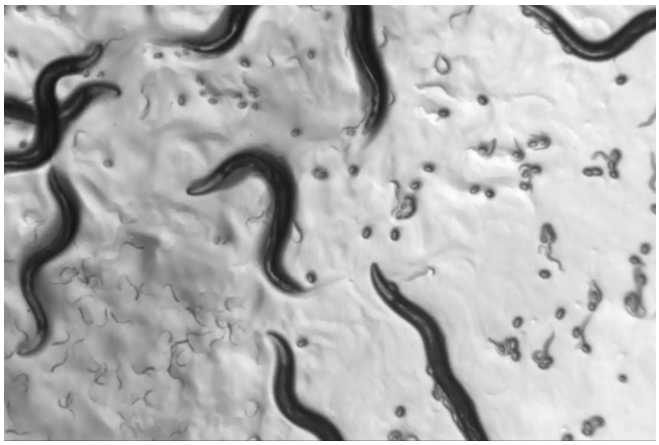

Movie S2. WT worms on *hmgs-1* RNAi with 20 mM mevalonate. A movie of 30 frames per second showing day-1 adult WT worms grown from egg to adulthood on *hmgs-1* RNAi in the presence of 20 mM mevalonate. The severe *hmgs-1* RNAi phenotypes shown in Movie S1 are fully rescued by the supplementation of mevalonate. This rescue demonstrates that *hmgs-1* knockdown phenotypes stem from an impaired mevalonate pathway flux. This result links HMGS-1 activity directly to the mevalonate pathway.

Movie S2

Other Supporting Information Files

Dataset S1 (XLSX)